

# Gravitational wave snapshots of generic extreme mass ratio inspirals

Steve Drasco

*Jet Propulsion Laboratory, California Institute of Technology, Pasadena, CA 91109 and  
Center for Radiophysics and Space Research, Cornell University, Ithaca, NY 14853*

Scott A. Hughes

*Department of Physics and MIT Kavli Institute,  
MIT, 77 Massachusetts Ave., Cambridge, MA 02139*

Using black hole perturbation theory, we calculate the gravitational waves produced by test particles moving on bound geodesic orbits about rotating black holes. The orbits we consider are generic — simultaneously eccentric and inclined. The waves can be described as having radial, polar, and azimuthal “voices”, each of which can be made to dominate by varying eccentricity and inclination. Although each voice is generally apparent in the waveform, the radial voice is prone to overpowering the others. We also compute the radiative fluxes of energy and axial angular momentum at infinity and through the event horizon. These fluxes, coupled to a prescription for the radiative evolution of the Carter constant, will be used in future work to adiabatically evolve through a sequence of generic orbits. This will enable the calculation of inspiral waveforms that, while lacking certain important features, will approximate those expected from astrophysical extreme mass ratio captures sufficiently well to aid development of measurement algorithms on a relatively short timescale.

PACS numbers: 04.70.-s, 97.60.Lf

## I. INTRODUCTION

One of the leading problems in modern general relativity research is the analysis of binary systems. This problem is quite nasty in general, especially when the members of the binary are strongly interacting and gravitational-wave (GW) emission is significant. It simplifies considerably in the extreme mass ratio limit, in which one member of the binary is much smaller than the other (taken to be a black hole). This is largely because the small mass ratio makes it possible to bring perturbative techniques to bear.

This paper reports the development of a key piece of infrastructure needed for an approximate approach to this problem: the ability to accurately calculate the instantaneous GW emission from arbitrary bound geodesic orbits of rotating Kerr black holes. Our work generalizes previous calculations which specialized the orbit to be either circular (of constant Boyer-Lindquist coordinate radius [1]) or equatorial (confined to the black hole’s plane of reflection symmetry [2]).

By knowing the GWs, we also calculate the flux of energy  $E$  and axial angular momentum  $L_z$  that the radiation carries to infinity and down the black hole’s event horizon. Global conservation allows us to evolve the energy and angular momentum associated with the orbit, fixing the evolution of two of the three “constants” which characterize black hole orbits (up to initial conditions). The remaining constant,  $Q$ , is known as the Carter constant<sup>1</sup> [3, 4]. In the limit of zero black hole spin, the hole

is spherically symmetric, geodesic orbits conserve total angular momentum  $L$ , and Carter’s constant is given by  $Q = L^2 - L_z^2$ ; though not strictly accurate, the intuitive interpretation “ $Q =$  the rest of the angular momentum” is useful even for non-zero black hole spin. It has recently become clear that, when the system evolves “slowly” (quantified below), it is possible to fix the evolution of  $Q$  using techniques not too different from those used to evolve  $E$  and  $L_z$  [5, 6, 7, 8].

For such slowly evolving systems, we can then evolve *all* of the orbital constants; by doing so, we can build reasonably realistic inspirals corresponding to generic initial conditions, as well as the associated waveforms. The qualifier “reasonably realistic” refers to the fact that this procedure neglects, by construction, the influence of “conservative” pieces of the small body’s self interaction; only the “dissipative” influence can be analyzed in this way. As we discuss further below, neglect of the conservative influence will limit the reliability of our inspirals; for the applications we have in mind, this limitation is a reasonable trade off in order to build waveforms on a rapid timescale.

We now briefly summarize our major motivations for analyzing this problem, sketch the techniques that we have developed and our major results, and discuss the utility and limitations of our results.

### A. Astrophysical context

Though an idealization of a much more difficult general problem, the extreme mass ratio limit in fact corresponds precisely to an important subset of astrophysical binaries: stellar mass compact objects captured onto highly

---

<sup>1</sup> The constant  $K = Q + (L_z - aE)^2$  is often used as well.

relativistic orbits of massive black holes in galaxy cores. Such binaries are expected to be created by multibody scattering processes in the stellar cluster that surrounds these central black holes.

It has now become clear that the central bulges of essentially all galaxies contain a massive black hole with properties strongly correlated to that of the bulge [9, 10]. It also appears likely that *mass segregation* (the sinking of massive stellar objects to the bottom of a gravitational potential due to equipartition of kinetic energy [11]) is likely to drive the largest stellar mass compact objects into the vicinity of the massive black hole, increasing the probability of forming a capture binary — see, for example, Ref. [12] for discussion pointing to the possibility of a “minicluster” of stellar mass black holes in the center of our galaxy, and Ref. [13] for evidence of an overabundance of black holes in binaries in the galaxy’s inner parsec. Mass segregation is also seen numerically in galactic center N-body simulations by Freitag [14]. The abundance of galactic black holes plus mass segregation suggest that the capture and GW driven inspiral of stellar mass compact objects into massive black holes may be a relatively common phenomenon in the universe.

The GWs produced by these *extreme mass ratio inspirals* (EMRIs) are thus ideal targets for low-frequency GW detectors, particularly the space-based *LISA* antenna, currently under development as a joint NASA-ESA mission [15, 16]. By combining estimates for the rate at which such captures are likely to occur (per galaxy) with the projected sensitivity of *LISA* (which determines the distance to which sources can be measured, and hence sets the number of galaxies that are relevant), one finds that dozens to thousands of EMRI events may be measured over *LISA*’s mission lifetime [17].

Because the small body only slightly perturbs the spacetime of the large black hole, the GWs are largely set by — and therefore encode — the nature of the black hole’s spacetime. A typical measured EMRI event is likely to last for  $\sim 10^4 - 10^5$  orbits; by coherently tracking the waveform’s phase over these orbits, *LISA* should determine parameters characterizing the binary with great precision. Black hole masses and spins should be measured with fraction of a percent accuracy or better [18]; it should even be possible to check whether the spacetime has the “shape” (higher multipolar structure) required by the no-hair theorems of general relativity [19, 20, 21]. EMRI measurements are expected to provide a cornucopia of data of interest to astrophysicists and general relativists.

This promising astrophysical scenario is a major motivator for much of the effort in this problem (certainly for the present authors). Reliable theoretical models of the inspiral waves will be needed both in order to maximize the science return from *LISA* data, but also to assure detection of these events. Ideally, the final science measurement of a detected signal will be performed with a “measurement template” — a model waveform computed accurately enough that it remains in phase with a frac-

tional accuracy of roughly  $1/\rho$  (where  $\rho$  is the measured signal-to-noise ratio) over the entire inspiral. The techniques which we describe here cannot construct waveforms accurate enough for this task; as we describe in Sec. IC, measurement templates require a more accurate and complete analysis of the small body’s self-interaction than our techniques encompass.

Our goal instead is to develop waveform models that are sufficiently reliable that they may be used to develop data analysis techniques for EMRI *detection*. EMRI waveforms are characterized by 14 parameters<sup>2</sup>. The number of measurement templates that would be needed to fully cover the 14 dimensional manifold of waveforms would render any search for these waves by this method infeasible [17]. Detection will instead be done hierarchically using (relatively) short segments of the EMRI signal [17]. Each short segment need only match coherently to a model for about  $10^3 - 10^4$  orbits. The accuracy requirements on such “detection templates” are less stringent than those needed for measurement templates.

## B. Sketch of our calculation

The key pieces of our formalism have been summarized in depth in previous papers, particularly [1]; here, we provide a very brief sketch largely to set the context for the following discussion.

We use the Teukolsky equation [22] to calculate the influence of a perturbation to a black hole spacetime. This equation describes the evolution of a complex scalar  $\psi_4$  which is constructed from the Weyl (vacuum) curvature of the spacetime; it is basically a wave equation for the Weyl curvature, linearized around the Kerr background<sup>3</sup>, with a source. Schematically, the Teukolsky equation is of the form

$$\mathcal{D}^2 \psi_4 = \mathcal{T}[\bar{z}(t)] . \quad (1.1)$$

The general form of the operator  $\mathcal{D}^2$  and the source function  $\mathcal{T}$  can be found in [22];  $\bar{z}(t)$  represents the worldline of the orbiting body. Coordinate time  $t$  (which amounts to time as measured by distant observers) is a particularly convenient parameterization for our purposes. Derived forms of Eq. (1.1) relevant to our analysis are given in Sec. III A.

<sup>2</sup> A useful counting of these parameters is as follows: the 2 masses, the black hole spin  $\mathbf{S}$ , the initial relative position  $\mathbf{r}_0$ , the initial relative velocity  $\mathbf{v}_0$ , and the binary’s position relative to the observer  $\mathbf{R}$ . Each vector has 3 components, for a total of 14 parameters. Including the smaller body’s spin  $\mathbf{s}$  raises the count to 17; fortunately,  $\mathbf{s}$  can be neglected for our purposes [18].

<sup>3</sup> Indeed, Michael Ryan has shown that the Teukolsky equation can be derived from the “Penrose equation” [23], a nonlinear wave equation for the Riemann curvature tensor that is constructed from the Bianchi identity; see [24].

A key thing to note at this point is that the source depends on the orbiting body’s worldline  $\vec{z}(t)$ . In order to construct  $\mathcal{T}$ , we use the “zeroth” order worldline, neglecting radiation. This worldline is built from geodesics of the background black hole spacetime; as we discuss in Sec. IC, we incur an important cost due to this setup. From this worldline, we build the source function, and then compute  $\psi_4$ . This complex scalar completely encodes the GW flux to distant observers, and down the black hole’s event horizon [25] (equivalently, the tidal interaction of the hole with the orbiting body [26]). All of the quantities which we use to describe GW emission and GW induced orbit evolution are encoded in  $\psi_4$ .

We take advantage of the fact that the Teukolsky equation is separable —  $\psi_4$  can be expanded into Fourier and spheroidal harmonics, allowing it to be computed mode-by-mode. Each mode is characterized by a spherical-harmonic-like integer index  $l$ , and by three integer indices  $(m, k, n)$  that label harmonics of the three fundamental frequencies that describe the orbits. Thanks to the linear nature of the Teukolsky equation, the modes are independent of one another. Codes that solve for  $\psi_4$  in this manner are thus easily parallelized — many mode contributions can be computed separately and independently. Indeed, we have found that the code developed for this work exhibits almost perfect  $1/N$  computation-time scaling (where  $N$  is the number of processors) [6].

We incur an important cost by expanding  $\psi_4$  in modes: expanding formally requires that we understand our source’s behavior for all time,  $-\infty < t < \infty$ , in order that the Fourier integral exist. In practice, this means that the orbit cannot evolve “quickly”: we require the radiation to backreact *adiabatically*, so that over a typical “orbital time”  $T_{\text{orb}}$  the change in any parameter that should be constant is much smaller than the parameter itself (e.g.,  $T_{\text{orb}}\dot{E} \ll E$ ). In principle, the adiabaticity requirement could be circumvented by working in the time domain — solving the wave equation for  $\psi_4$  directly rather than expanding in modes. Indeed, time domain codes have proven superior to frequency domain codes for analyzing problems without sources (i.e. black hole ringdown), and are a more natural approach to evolving radiation propagating in a black hole spacetime [27, 28, 29, 30]. Although new techniques may eventually change this story [31], at present, frequency domain codes appear better suited to handle the point-like sources appropriate to the EMRI problem.

The next natural step is to approximate the inspiral and associated waveform from a sequence of geodesic orbits. Beginning with some starting orbit, we compute  $\psi_4$ . From it, we extract a snapshot waveform, which instantaneously approximates the true waveform, as well as the rates of change of the orbital constants. These rates of change tell us how the trajectory evolves from the present orbit to the next orbit in the sequence. By repeating this process many times, we can build an adiabatic waveform that usefully approximates the true waveform. We have not yet taken this step for generic orbits, though most of

| Ref.    | $a \neq 0$ | eccentric orbits | inclined orbits | evolve orbits |
|---------|------------|------------------|-----------------|---------------|
| [32]    |            | ✓                | ...             | ✓             |
| [33]    | ✓          |                  |                 | ✓             |
| [1, 34] | ✓          |                  | ✓               |               |
| [2, 35] | ✓          | ✓                |                 |               |
| [36]    | ✓          |                  | ✓               | ✓             |
| Here    | ✓          | ✓                | ✓               |               |

TABLE I: A sketch of the history of this technique. The magnitude of the massive black hole’s spin angular momentum is given by  $aM$ . Due to spherical symmetry all geodesics of Schwarzschild ( $a = 0$ ) black holes are planar, and can be considered equatorial.

the tools needed to do so are now in hand [5, 6, 7, 8].

Table I summarizes the history of this approach. To date, the program has been completed only for non-spinning black holes [32], circular-equatorial orbits [33] circular orbits [36], and equatorial orbits<sup>4</sup> [2, 35]. For the astrophysical EMRI problem, these are unrealistic restrictions. Since extreme mass ratio binaries are created through capture processes, we expect inclination to be randomly distributed. We also expect the eccentricity to be substantial — although radiative backreaction strongly reduces eccentricity, EMRI events have such large initial eccentricities that an estimated 50% of all observable EMRIs will have eccentricities  $e > 0.2$  as they approach their last stable orbit [18]. We must understand generic EMRIs in order to realize the event rates predicted in Ref. [17].

### C. Applicability and limitations of our approach

The “flux balancing-adiabatic evolution” approach we advocate here is, as emphasized above, an approximation to the evolution of extreme mass ratio binaries. A more rigorous approach, upon which most workers in this field are focused, is based on computation of the *self force* — the small body’s self interaction with its own gravitational perturbation. The gravitational self force is analogous to the Abraham-Lorentz-Dirac electromagnetic self force [37, 38]. Its complete general relativistic formulation was worked out in detail by Mino, Sasaki, and Tanaka [39] and by Quinn and Wald [40]; Poisson [41] provides a very readable summary of this formalism. Developing this approach to the point that one can build a code around it to study the evolution of generic orbits of Kerr black holes remains some time in the future; however, efforts are intense and progress is rapid [42].

<sup>4</sup> Although Refs. [2] and [35] do not use their snapshot data to compute model inspirals, it is a straightforward extension to do so.

At least heuristically, the self force can be broken into two pieces: a “dissipative” force which carries energy and angular momentum away from the binary (and thus drives the smaller body’s inspiral), and a “conservative” force which does not. These forces are computed relative to geodesics of the *background* spacetime — the spacetime of the large black hole. The conservative force tells us that, even in the absence of radiation emission, the trajectory is modified relative to the background geodesics — the spacetime is deformed from that of a black hole, so that black hole geodesics do not precisely describe the motion of the small body.

Our approach totally neglects the conservative self force — by construction, we can only analyze dissipative effects. This can be seen in the schematic description of our calculation near Eq. (1.1) — the worldline used in the source function  $\mathcal{T}$  is built from geodesics of the *background* spacetime, without incorporating the influence of the conservative force. We have argued previously [6] that this should be adequate for scoping out EMRI waveforms and exploring issues related to *LISA* data analysis. Our argument was based in part on how the phase error resulting from our approach scales with the mass ratio  $\mu/M$  [Eq. (1.2) of Ref. [7]]. That scaling was in turn based on the idea that (quoting from Ref. [6]) “*Dissipative terms accumulate secularly; conservative terms do not*”. In other words, dissipative aspects of the self force would accumulate phase effects over an EMRI event; we expected that conservative terms would oscillate, and thus not contribute as strongly over an inspiral.

To our chagrin, it has now been clearly demonstrated that our claim that conservative effects do not accumulate secularly is wrong (although the scaling of phase errors with mass ratio which we derived from this is correct). Using a compelling toy model to describe the influence of the conservative self force, Pound, Poisson, and Nickel [43] show that there is a component to the phase evolution missed by a “dissipative only” evolution. A simple way to understand this additional component is as follows: The background geodesics are characterized by oscillatory motion with three frequencies,  $\Omega_\phi$ ,  $\Omega_\theta$ , and  $\Omega_r$ , where  $\Omega_x$  describes oscillations (or orbits) associated with the coordinate  $x$ . A conservative self force changes the “potentials” that determine orbital motion, and thus modifies these three frequencies:

$$\begin{aligned}\Omega_\phi &\rightarrow \Omega_\phi + \delta\Omega_\phi \\ \Omega_\theta &\rightarrow \Omega_\theta + \delta\Omega_\theta \\ \Omega_r &\rightarrow \Omega_r + \delta\Omega_r .\end{aligned}\tag{1.2}$$

The shifts are smaller than their frequencies by (roughly) the mass ratio:  $\delta\Omega_x \sim (\mu/M)\Omega_x$ , where  $\mu$  is the mass of the smaller body and  $M$  is the mass of the black hole.

Some of the most interesting strong field features are due to beating between these frequencies. For example, periastron precession (well known in the solar system due

to planetary perihelion precession) occurs at

$$\Omega_{\text{PP}} = \Omega_\phi - \Omega_r .\tag{1.3}$$

Another effect is Lense-Thirring precession, the rotation of the orbital plane due to frame dragging; it occurs at

$$\Omega_{\text{LT}} = \Omega_\phi - \Omega_\theta .\tag{1.4}$$

The conservative self force shifts these precessions:

$$\begin{aligned}\delta\Omega_{\text{PP}} &= \delta\Omega_\phi - \delta\Omega_r , \\ \delta\Omega_{\text{LT}} &= \delta\Omega_\phi - \delta\Omega_\theta .\end{aligned}\tag{1.5}$$

It is likely that  $\delta\Omega_\phi \simeq \delta\Omega_\theta$ ; they are presumably exactly equal for Schwarzschild black holes (spherical symmetry). However,  $\delta\Omega_r$  is likely to differ quite a bit from the other two frequency shifts, importantly modifying periastron precession. We thus expect that eccentric orbits in particular will be impacted by the conservative self force. This, indeed, is what is found by Pound, Poisson, and Nickel.

Our inability to incorporate this conservative effect into our analysis limits its utility. We advocate our approach primarily to begin exploring the space of EMRI waveforms in preparation for *LISA*’s EMRI data analysis. The best understanding at the moment, after Ref. [43], is that the phase errors scale like  $(\mu/M)^0$  and  $(v/c)^{-3}$ ; consequently, in the regime  $v \sim c$  relevant to *LISA* the errors are formally of order unity. It is thus not yet clear if these errors are large enough to prevent adiabatic waveforms being useful for search templates. At any rate, though adiabatic waveforms may miss an important contribution to the phase evolution of extreme mass ratio binaries, they accurately represent the spectral spread that can be expected. Experience from circular [1, 36] and equatorial [2, 32] studies shows that waves from strong field orbits radiate significant power into high harmonics of the orbital frequencies. The *LISA* datastream is expected to contain many simultaneous confused sources — certainly millions of white dwarf binaries (whose radiation is essentially monochromatic), perhaps  $\sim 10^3$  simultaneous EMRI sources, all lying under the signals from massive coalescing cosmological black hole binaries. Learning to detangle these many signals will require models for the different waves which accurately describe their time and frequency overlap. By modeling the frequency spread of EMRI waves with good accuracy (though not necessarily the frequency evolution), adiabatic waveforms should be a very useful tool.

If it turns out to be possible to separate conservative and dissipative self force contributions, it should be easy to modify our approach to include the leading conservative effects: we would simply replace the geodesic worldlines presently used with worldlines that are augmented by these conservative effects. We would then use this augmented worldline to construct the Teukolsky source function. Doing so would allow us to calculate an inspiral

that accurately accounted for the leading dissipative *and* conservative effects<sup>5</sup>.

It should be strongly emphasized that this is a rather big “if”: Because the gravitational self force is a gauge dependent quantity (though its impact on binary orbits must be gauge independent), it is far from clear that one can cleanly separate the “conservative” from the “dissipative” influence. It may be that the only way to discriminate the two influences is to run the equations of motion which the self force implies through a self-consistent wave-generation calculation [43], in which case there is no need to separate these influences in the first place.

#### D. Organization of this paper

We begin this paper by summarizing, in Sec. II, relevant properties of bound Kerr black hole orbits. These orbits determine, in turn, the properties of the Teukolsky equation’s source term. Our goal is to present enough detail to make it clear how we build this term. Of particular importance is a frequency domain description of functions that are built from these orbits [44, 45].

We next (Sec. III) summarize the relevant details of the black hole perturbation formalism that we use. We go into some detail in this section. This is in part to make the analysis self-contained, but also to correct some small errors that have appeared in previous papers, notably Ref. [1] (hopefully without introducing too many new errors). We first review in Sec. III A how Teukolsky equation solutions are built. This is a somewhat subtle numerical problem — due to the long-rangedness of the separated Teukolsky equation’s radial potential, the amplitudes of ingoing ( $\propto e^{-i\omega r^*}$ ) and outgoing ( $\propto e^{i\omega r^*}$ ) radiative solutions grow at different rates. [The quantity  $r^*$  is the Kerr “tortoise coordinate”; cf. Eq. (3.16) below.] One component of the solution can easily swamp the other, causing numerical resolution to be lost. Sasaki and Nakamura [46] found an equation with short-ranged potential whose solutions are related to those of the Teukolsky equation by a simple differential transformation; the combined Sasaki-Nakamura-Teukolsky formalism makes for a very well-behaved numerical problem. We next (Sec. III B) discuss explicitly how the source function is built, taking advantage of the results that we presented in Sec. II, and then discuss some practical issues related to the numerics (Sec. III C). We wrap up this section with a brief discussion of how the gravitational waveforms and fluxes of “conserved” quantities are extracted from these solutions.

Section IV discusses several practical issues related to numerics. We first describe the algorithms used to numerically represent the geodesics, a key element for the

Teukolsky source term, before describing issues related to computing each of the modes from which we build  $\psi_4$ . We then discuss in great depth the algorithms we have developed to truncate our modal expansion. Strictly speaking, the number of modes that should be used to build  $\psi_4$  is infinite; picking a finite value to truncate this expansion that is “large enough” is somewhat subtle. We describe a scheme in Sec. IV C that has proven to be robust enough to work well for our present purposes. There is clearly room for improvement, however; we describe some ways in which this procedure could be made better. Finally, we conclude in Sec. IV D with detailed discussion of validation tests that we made against previous results in the appropriate limits. We find that the code agrees perfectly with results from Ref. [1] when the eccentricity is zero<sup>6</sup>, and agrees quite well with the “equatorial” code of Glampedakis and Kennefick in [2] in the limit of zero inclination. Except for some (very small) down-horizon modes that do not significantly impact the overall flux, we typically find agreement at the level of  $10^{-3}$  or better with Glampedakis and Kennefick. This is the level of accuracy that they cite for their code.

Our main results are presented in Sec. V. The modal decomposition allows us to break the waveform into “voices”:

$$H \equiv h_+ - ih_\times = \sum_{kn} H_{kn} e^{-i\omega_{kn}(t-r^*)}, \quad (1.6)$$

where  $\omega_{kn} \equiv k\Omega_\theta + n\Omega_r$ . [A sum over  $l$  and  $m$ , including oscillations with frequency  $m\Omega_\phi$ , is hidden in the definition of  $H_{kn}$ ; see Eq. (5.3) below.] The “polar voice” is composed of the terms with  $n = 0$  and  $k \neq 0$ ; The “radial voice” is composed of the terms with  $k = 0$  and  $n \neq 0$ ; The “azimuthal voice” is the term with  $k = n = 0$ , and the “mixed voice” is composed of the terms with  $k \neq 0$  and  $n \neq 0$ . A similar voice-by-voice labeling can be applied to the fluxes. We find that the importance of the various voices is fairly simply controlled by the eccentricity and the inclination angle: Polar voices become progressively more important as the purely polar orbit (inclination  $90^\circ$ ) is approached from either direction; radial voices rapidly become important as eccentricity,  $e$ , approaches unity, typically dominating the waves’ spectrum by  $e \sim 0.3 - 0.5$ . We speculate that this multivoice character may facilitate approximations in the design of GW detection schemes, making it possible to detect the most important voices of signals, rather than needing to detect the (rather ornate) chorus of all voices together.

Section VI presents our final conclusions, and outlines future work to which we plan to apply this formalism.

<sup>5</sup> One might label a self force that allows this separation “compassionately conservative”.

<sup>6</sup> The “generic” code is a direct descendent of the “circular” code used in Ref. [1], so it is perhaps not too surprising that there is agreement in the circular limit. However, *many* details of the generic code’s inner workings are significantly different from the circular incarnation, so this agreement is far from trivial.

Chief among these future tasks will be augmenting this approach with an adiabatic scheme to evolve the Carter constant [7, 8], and then using the complete flux data to build model adiabatic inspirals and their associated waveforms (as discussed in Sec. IB). We are optimistic that this can be completed relatively quickly since there appear to be no major hurdles or issues of principle that must be overcome first. Producing adiabatic waveforms for initial data analysis algorithm development will then “just” be a matter of finding sufficient CPU power.

## II. BOUND BLACK HOLE ORBITS

In this section we review the geodesic motion of a non-spinning test mass on a bound orbit of a Kerr black hole. Kerr orbits are not a new subject of investigation [4, 47], but interest has been renewed recently because of their relevance to EMRI GWs [5, 44, 45]. The main new development has been Mino’s exploitation of the fact that these orbits are fundamentally periodic entities [5]. The utility of exploiting this property is discussed in detail in Ref. [44], and details of its application to EMRIs can be found in Sec. 3 of Ref. [7]. Here we will discuss the relation between an orbit’s geometry and its natural frequencies. Using a special choice of initial conditions (the fiducial geodesics from Ref. [7]) we also derive a new system of equations for efficient numerical evaluation of these orbits.

Kerr black holes are characterized by two parameters: the mass  $M$  of the black hole, and the magnitude  $aM$  of its spin angular momentum, with  $0 \leq a \leq M$ . Throughout this paper, we will use Boyer-Lindquist [48] coordinates  $(t, r, \theta, \phi)$ , with units chosen so that  $G = c = 1$ . The line element for the Kerr geometry is then given by [3]

$$ds_{\text{Kerr}}^2 = - \left( 1 - \frac{2Mr}{\Sigma} \right) dt^2 + \frac{\Sigma}{\Delta} dr^2 + \Sigma d\theta^2 + \left( r^2 + a^2 + \frac{2Ma^2r}{\Sigma} \sin^2 \theta \right) \sin^2 \theta d\phi^2 - \frac{4Mar}{\Sigma} \sin^2 \theta dt d\phi, \quad (2.1)$$

where

$$\Sigma = r^2 + a^2 \cos^2 \theta, \quad \Delta = r^2 - 2Mr + a^2. \quad (2.2)$$

Bound black hole orbits admit four constants of the motion which allow us to rewrite the geodesic equations as a system of first order differential equations. Three of these constants are fairly straightforward — if the test particle has 4-momentum  $\vec{p}$ , these constants are

$$\vec{p} \cdot \vec{p} = -\mu^2, \quad \vec{\partial}_t \cdot \vec{p} = -E, \quad \vec{\partial}_\phi \cdot \vec{p} = L_z, \quad (2.3)$$

where  $\mu$  is its rest mass,  $E$  is the orbit’s energy, and  $L_z$  is its axial angular momentum. Carter discovered a fourth constant  $Q$  which allows the motion to be completely

described by a system of first order equations [4]. As discussed in the Introduction, it is often useful to think of the Carter constant as representing the geodesic’s non-axial angular momentum (a correspondence which is exact for non-rotating black holes).

Carter’s first order equations can be written in the following form

$$\begin{aligned} \left( \frac{dr}{d\lambda} \right)^2 &= V_r(r), & \frac{dt}{d\lambda} &= V_t(r, \theta), \\ \left( \frac{d\theta}{d\lambda} \right)^2 &= V_\theta(\theta), & \frac{d\phi}{d\lambda} &= V_\phi(r, \theta). \end{aligned} \quad (2.4)$$

The functions  $V_t$ ,  $V_r$ ,  $V_\theta$ , and  $V_\phi$  are shown in Appendix A. The Mino time parameter  $\lambda$  is related to the test mass’ proper time  $\tau$  by

$$\frac{d\tau}{d\lambda} = \Sigma. \quad (2.5)$$

Mino time decouples the radial and polar equations of motion so that  $V_r = V_r(r)$  and  $V_\theta = V_\theta(\theta)$ . This property appears to have been recognized by Carter; however, Mino appears to be the first to use  $\lambda$  to fully exploit the periodic nature of Kerr orbits [5]. Since the first order equations for  $r$  and  $\theta$  are purely quadratic in their derivatives,  $r(\lambda)$  and  $\theta(\lambda)$  are periodic functions for bound orbits. The functions  $dt/d\lambda$  and  $d\phi/d\lambda$  are then biperiodic functions in the sense defined by Ref. [44]. As a result, after subtracting a term proportional to  $\lambda$ , the coordinates  $t(\lambda)$  and  $\phi(\lambda)$  can be represented with a two dimensional Fourier series. These properties, discussed in more detail below, are extremely powerful.

Solutions of the geodesic equations (2.4) are uniquely determined if we specify  $E$ ,  $L_z$ ,  $Q$  and the initial position  $\vec{z}(\lambda = 0)$  (or some other equivalent set of constants). We now focus on the orbit’s geometry or shape, which is determined by  $E$ ,  $L_z$ , and  $Q$ . This fact can be roughly understood in that the orbit must be bounded by two radii  $r_{\min} \leq r \leq r_{\max}$ , and [because the geometry (2.1) is symmetric across the equatorial plane] one polar angle  $\theta_{\min} \leq \theta \leq (\pi - \theta_{\min})$ . The orbit is then confined to a toroidal region sketched in Fig. 1. The boundaries of the orbital torus could have equivalently been determined by an eccentricity  $e$ , a semilatus rectum  $p$ , and an inclination  $\theta_{\text{inc}}$  defined by

$$r_{\min} = \frac{pM}{1+e}, \quad r_{\max} = \frac{pM}{1-e}, \quad \theta_{\text{inc}} + (\text{sgn } L_z)\theta_{\min} = \frac{\pi}{2}. \quad (2.6)$$

Here we have included a factor of  $\text{sgn } L_z$  so as to make  $\theta_{\text{inc}}$  most closely resemble another common definition for the orbital inclination angle  $\iota$  [1]:

$$\cos \iota = \frac{L_z}{\sqrt{L_z^2 + Q}}. \quad (2.7)$$

A nice property of the angles  $\theta_{\text{inc}}$  and  $\iota$  (not shared by the angle  $\theta_{\min}$ ) is that they automatically encode a notion of

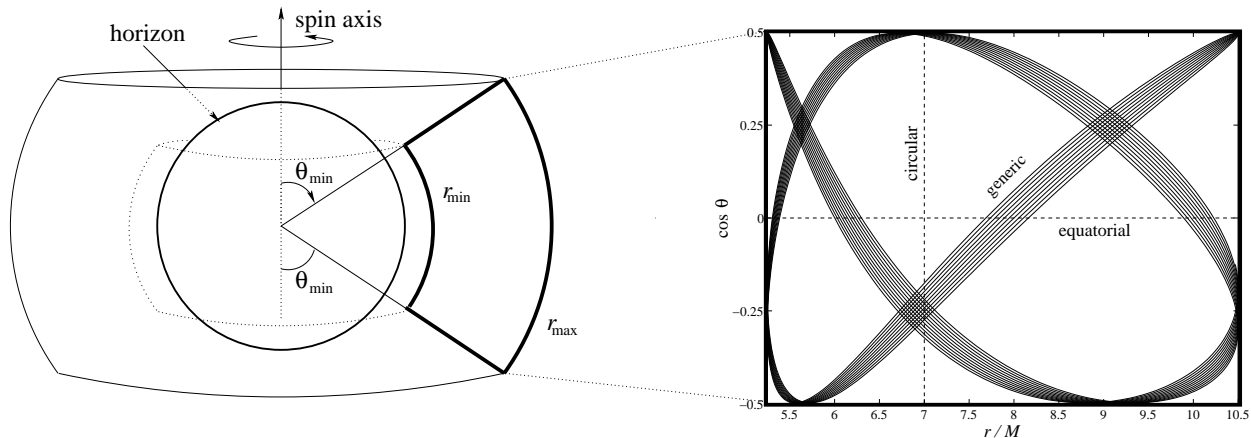


FIG. 1: The orbital torus and the evolution of  $r$  and  $\cos \theta$  for a generic geodesic orbit. The magnitude of the black hole's spin is  $a = 0.998M$ . The orbit shown here has eccentricity  $e = 1/3$ , inclination  $\theta_{\text{inc}} = 30^\circ$ , and semilatus rectum  $p = 7$ . We start the orbit at  $(r, \cos \theta) = (r_{\text{min}}, \cos \theta_{\text{min}})$ , and end it around  $(r, \cos \theta) = (10.5M, -0.1)$ , after several complete radial and polar oscillations. The orbit is not closed: over time, it would eventually fill the orbital torus.

prograde and retrograde — prograde orbits ( $\phi$  motion parallel to the hole's rotation) have  $\theta_{\text{inc}, \iota} < 90^\circ$ ; retrograde orbits ( $\phi$  motion antiparallel to the hole) have  $\theta_{\text{inc}, \iota} > 90^\circ$ . We have found that in general  $\iota \approx \theta_{\text{inc}}$ . Even in the strong field the two quantities typically differ by less than 10%. For the orbits which we discuss in detail here (Sec. V)  $\iota$  and  $\theta_{\text{inc}}$  differ by no more than 0.5%.

Explicit algebraic relationships between the geometric orbital parameters  $(e, p, \theta_{\text{inc}})$  and the physical constants  $(E, L_z, Q)$  were first computed by Schmidt [45], and are shown below in Appendix A. We find that when exploring the orbital parameters space, it is best to first think in terms of  $(e, p, \theta_{\text{inc}})$ , and then to convert these (following Appendix A) to  $(E, L_z, Q)$  which are used in all further calculations.

Using a special choice of initial conditions, we now derive a set of equations for efficient numerical evaluation of bound orbits. Since the solutions to the radial and polar geodesic equations (2.4) are periodic in Mino time, each can be expressed as a Fourier series,

$$\theta(\lambda) = \sum_{k=-\infty}^{\infty} \theta_k e^{-ik\Upsilon_\theta \lambda}, \quad r(\lambda) = \sum_{n=-\infty}^{\infty} r_n e^{-in\Upsilon_r \lambda}, \quad (2.8)$$

where  $\theta_k$  and  $r_n$  are constants, and where  $\Upsilon_{r, \theta}$  are the orbital frequencies in Mino time. In Appendix A we list explicit expressions for these frequencies as functions of the orbital parameters described in the previous section. It is convenient to write these series in terms of angle-variables,

$$w_r = \Upsilon_r \lambda, \quad w_\theta = \Upsilon_\theta \lambda. \quad (2.9)$$

The result is

$$\theta(w_\theta) = \sum_{k=-\infty}^{\infty} \theta_k e^{-ikw_\theta}, \quad r(w_r) = \sum_{n=-\infty}^{\infty} r_n e^{-inw_r}. \quad (2.10)$$

We now specialize to a specific choice of initial conditions for the radial and polar motion. We require that the orbit begins at a turning point of both the  $r$  and  $\theta$  coordinates,

$$r(w_r = 0) = r_{\text{min}}, \quad \theta(w_\theta = 0) = \theta_{\text{min}}. \quad (2.11)$$

This choice of initial conditions will result in a simplified numerical evaluation of the geodesics. For example, the coordinates  $r$  and  $\theta$  are now even functions of  $w_{r, \theta}$ ,

$$r(-w_r) = r(w_r), \quad \theta(-w_\theta) = \theta(w_\theta), \quad (2.12)$$

and the Fourier series (2.8) become cosine series,

$$\theta(w_\theta) = \theta_0 + 2 \sum_{k=1}^{\infty} \theta_k \cos(kw_\theta), \quad (2.13)$$

$$r(w_r) = r_0 + 2 \sum_{n=1}^{\infty} r_n \cos(nw_r). \quad (2.14)$$

In this paper we will not evaluate these series explicitly<sup>7</sup>, though we will use the fact that they are even functions.

We now derive a similarly simplified series expansion for  $t$  and  $\phi$ . Both the  $t$  and  $\phi$  coordinates will be treated

<sup>7</sup> Current investigations suggest that doing so may lead to greater computational efficiency.

in a similar way, so to save space we define

$$x = t, \phi, \quad \dot{x} = V_t, V_\phi, \quad (2.15)$$

such that an overdot represents a derivative with respect to Mino time  $\lambda$ . Following the analysis preceding Eqs. (3.18) and (3.19) in Ref. [44], we write the derivatives  $\dot{x}$  in the form

$$\begin{aligned} \dot{x}(\lambda) &= \dot{x}_{00} + \sum_{k=1}^{\infty} (\dot{x}_k^\theta e^{-ik\Upsilon_\theta \lambda} + \text{c.c.}) \\ &\quad + \sum_{n=1}^{\infty} (\dot{x}_n^r e^{-in\Upsilon_r \lambda} + \text{c.c.}), \end{aligned} \quad (2.16a)$$

$$\dot{x}_k^\theta = \frac{1}{2\pi} \int_0^{2\pi} dw_\theta \dot{x}^\theta[\theta(w_\theta)] e^{ikw_\theta}, \quad (2.16b)$$

$$\dot{x}_n^r = \frac{1}{2\pi} \int_0^{2\pi} dw_r \dot{x}^r[r(w_r)] e^{inw_r}. \quad (2.16c)$$

Here ‘‘c.c.’’ means the complex conjugate of the preceding term. The leading constants are defined by

$$\dot{x}_{00} = \dot{x}_0^\theta + \dot{x}_0^r. \quad (2.17)$$

We have made use of the fact that the derivatives of both  $t$  and  $\phi$  separate into a sum of two functions, each depending only on one of the coordinates<sup>8</sup>,

$$\dot{x} = \dot{x}^\theta(\theta) + \dot{x}^r(r). \quad (2.18)$$

Following the notation of Ref. [44], we use the following symbols for  $\dot{x}_{00}$  in the cases  $x = t$  and  $x = \phi$ :

$$\Gamma = (V_t)_{00}, \quad \Upsilon_\phi = (V_\phi)_{00}. \quad (2.19)$$

The constant  $\Gamma$  is the analog of the Lorentz factor of special relativity. For example, in the case of an orbit which is both circular and equatorial, we have  $\Gamma = dt/d\lambda = (dt/d\tau)\Sigma$  ( $\Sigma$  is constant for circular-equatorial orbits).  $\Gamma$  also relates the Mino time frequencies  $\Upsilon_{\phi,\theta,r}$  to coordinate time frequencies  $\Omega_r, \Omega_\theta$ , and  $\Omega_\phi$ :

$$\Omega_\phi = \frac{\Upsilon_\phi}{\Gamma}, \quad \Omega_\theta = \frac{\Upsilon_\theta}{\Gamma}, \quad \Omega_r = \frac{\Upsilon_r}{\Gamma}. \quad (2.20)$$

Schmidt [45] provides an elegant derivation of closed form expressions for the orbital frequencies. His results were converted into the Mino time frequencies in Ref. [44] (see Appendix A for details).

As a consequence of their initial values (2.11), the functions  $\theta(w_\theta)$  and  $r(w_r)$  are even. The functions  $\dot{x}^\theta(w_\theta)$  and  $\dot{x}^r(w_r)$  are then also even, and the series (2.16) above

simplifies to

$$\dot{x}(\lambda) = \dot{x}_{00} + 2 \sum_{k=1}^{\infty} \dot{x}_k^\theta \cos(k\Upsilon_\theta \lambda) + 2 \sum_{n=1}^{\infty} \dot{x}_n^r \cos(n\Upsilon_r \lambda). \quad (2.21a)$$

$$\dot{x}_k^\theta = \frac{1}{\pi} \int_0^\pi dw_\theta \dot{x}^\theta[\theta(w_\theta)] \cos(kw_\theta), \quad (2.21b)$$

$$\dot{x}_n^r = \frac{1}{\pi} \int_0^\pi dw_r \dot{x}^r[r(w_r)] \cos(nw_r). \quad (2.21c)$$

If we now assume initial values for  $t$  and  $\phi$ ,

$$t(\lambda = 0) = 0, \quad \phi(\lambda = 0) = 0, \quad (2.22)$$

so that we are now discussing the fiducial geodesics from Ref. [7], a similarly simplified expression for the coordinates  $x$  can be found by integrating the series (2.21a) for their derivatives  $\dot{x}$ :

$$x(\lambda) = \dot{x}_{00}\lambda + \Delta x^\theta(\lambda) + \Delta x^r(\lambda) \quad (2.23a)$$

$$\Delta x^\theta(\lambda) = \sum_{k=1}^{\infty} \Delta x_k^\theta \sin(k\Upsilon_\theta \lambda), \quad (2.23b)$$

$$\Delta x^r(\lambda) = \sum_{n=1}^{\infty} \Delta x_n^r \sin(n\Upsilon_r \lambda), \quad (2.23c)$$

$$\Delta x_k^\theta = \frac{2}{k\pi\Upsilon_k} \int_0^\pi dw_\theta \dot{x}^\theta(w_\theta) \cos(kw_\theta), \quad (2.23d)$$

$$\Delta x_n^r = \frac{2}{n\pi\Upsilon_r} \int_0^\pi dw_r \dot{x}^r(w_r) \cos(nw_r). \quad (2.23e)$$

Note that in the cases of orbits with special geometries, the coordinates  $x$  simplify accordingly:

$$\Delta x^r(\lambda) = 0 = \Delta x_n^r \quad (\text{for circular orbits}), \quad (2.24a)$$

$$\Delta x^\theta(\lambda) = 0 = \Delta x_k^\theta \quad (\text{for equatorial orbits}). \quad (2.24b)$$

Evaluating the integrands in Eqs. (2.23d) and (2.23e) as functions of  $r(w_r)$  and  $\theta(w_\theta)$ , would first require a direct integration of the radial and polar geodesic equations. Unfortunately this is somewhat difficult because the derivatives  $V_r$  and  $V_\theta$  vanish (by definition) at the orbital turning points. This means, for example, that the integrand in the direct expression for  $r(\lambda)$ ,

$$\lambda = \int_{r_{\min}}^{r(\lambda)} \frac{dr'}{\pm \sqrt{V_r(r')}}}, \quad (2.25)$$

contains singularities which, although integrable, complicate the numerics. This is a well known problem (see the Appendix of Ref. [44] for more details) which can be avoided if we change the integration variables to more well behaved coordinates  $\chi(\theta)$  and  $\psi(r)$ , where

$$\cos \chi = \frac{\cos \theta}{\cos \theta_{\min}}, \quad r = \frac{pM}{1 + e \cos \psi}. \quad (2.26)$$

<sup>8</sup> It's interesting to note that Teukolsky has shown that the master equation (3.2) separates in any coordinates where this property (2.18) is preserved [22].

Recall that  $p$  is the semilatus rectum of the orbit, and  $e$  is the orbital eccentricity. So in practice we replace Eqs.(2.23d) and (2.23e) with

$$\Delta x_k^\theta = \frac{2}{k\pi\Upsilon_\theta} \int_0^\pi d\chi \frac{dw_\theta}{d\chi} \dot{x}^\theta(w_\theta) \cos(kw_\theta), \quad (2.27)$$

$$\Delta x_n^r = \frac{2}{n\pi\Upsilon_r} \int_0^\pi d\psi \frac{dw_r}{d\psi} \dot{x}^r(w_r) \cos(nw_r). \quad (2.28)$$

In order to use this result, we of course need explicit expressions for  $w_\theta(\chi)$ ,  $w_r(\psi)$ , and their derivatives. These functions were first derived in Ref. [44], and the results are shown below in Appendix A. It turns out that  $w_\theta(\chi)$  and  $dw_\theta/d\chi$  can be written in terms of elliptic integrals. The functions  $w_r(\psi)$  and  $dw_r/d\psi$  are slightly more involved.

We have found that this technique is an extremely efficient way to evaluate bound orbits and functions of them (see Ref. [44] for a simple example). The two expansions given by Eqs. (2.23b) and (2.23c) converge very rapidly. Typically only about 50 terms are needed in order to obtain a fractional accuracy of  $10^{-12}$ .

### III. PERTURBING A BLACK HOLE WITH AN ORBITING TEST MASS

In this section we will discuss how a non-spinning test mass  $\mu$  on a bound geodesic perturbs the Kerr geometry (2.1). The radiative information describing the linear order perturbation can be extracted from the Weyl curvature scalar [49]

$$\psi_4 = -C_{\alpha\beta\gamma\delta} n^\alpha \bar{m}^\beta n^\gamma \bar{m}^\delta. \quad (3.1)$$

Here, overbar denotes complex conjugation,  $C_{abcd}$  is the Weyl curvature tensor (the Riemann tensor in vacuum), and the vectors are elements of a Newman-Penrose null-basis [50, 51]  $\{l^\alpha, m^\alpha, \bar{m}^\alpha, n^\alpha\}$ . For distant observers, the curvature scalar  $\psi_4$  is simply related to the metric perturbation. For these same observers, and also for observers at the event horizon,  $\psi_4$  is simply related to the fluxes of energy and angular momentum (see Sec. IIID for details). Since we are only analyzing perturbations to first order in the mass ratio,  $\psi_4$  always represents the leading  $O(\mu/M)$  contribution to the curvature perturbation.

#### A. Teukolsky-Sasaki-Nakamura formalism

Teukolsky showed that  $\psi_4$  is a solution to an equation of the form [22]

$$\left[ \widehat{U}_{t\phi r}(r) + \widehat{V}_{t\phi\theta}(\theta) \right] \varphi = -\mathcal{T}, \quad (3.2)$$

where  $\mathcal{T}$  is the source term (described below in Sec. IIIB),

$$\varphi = \rho^{-4} \psi_4, \quad \rho = -(r - ia \cos \theta)^{-1}, \quad (3.3)$$

and where  $\widehat{U}_{t\phi r}(r)$  and  $\widehat{V}_{t\phi\theta}(\theta)$  are second order differential operators containing derivatives with respect to the variables shown as subscripts [see Eqs. (B1a) and (B1b)]. Equation (3.2) is known as the master equation. In the next two sections, we will summarize Teukolsky's technique for solving the master equation by separation of variables [22], converting Eq. (3.2) into a pair of ordinary differential equations. This technique is referred to as solving the master equation "in the frequency domain". As briefly discussed in the Introduction, one could instead solve the master equation numerically as a partial differential equation "in the time domain" (see Refs. [52, 53] and references therein). Such an approach can be advantageous for problems where there is no source, or where the source is not pointlike. To date at least, time domain treatments are accurate to about 10% [53] for EMRI sources (at least for quantities like orbit averaged fluxes of energy and angular momentum).

In the source free case  $\mathcal{T} = 0$ , the master equation (3.2) is satisfied by functions of the form

$$\varphi_m(\omega, C) = \widetilde{R}_m(r; \omega, C) S_m(\theta; \omega, C) e^{-i\omega t + im\phi}, \quad (3.4)$$

where  $C$  is some constant,  $m$  is an integer (since  $\psi$  must be periodic in  $\phi$ ), and  $\omega$  is any real number. The functions  $\widetilde{R}$  and  $S$  are solutions to ordinary differential equations of the form

$$\left[ \widehat{U}_r(r, m, \omega) - C \right] \widetilde{R}_m(r, \omega, C) = 0, \quad (3.5a)$$

$$\left[ \widehat{V}_\theta(\theta, m, \omega) + C \right] S_m(\theta, \omega, C) = 0. \quad (3.5b)$$

Requiring that the solutions to the angular equation (3.5b) (known as spin-weighted spheroidal harmonics with spin weight  $-2$ ) be regular results in a discrete spectrum of eigenvalues  $C = C_{lm}(\omega)$ ,

$$S_m[\theta, \omega, C_{lm}(\omega)] \equiv S_{lm}(\theta, \omega), \quad (3.6)$$

where  $l \geq \max(|m|, 2)$  is an integer. The functions  $S_{lm}(\theta, \omega)$  are uniquely defined only after we specify boundary conditions, or equivalently after we chose a normalization convention. We use the convention<sup>9</sup>

$$\int_0^\pi d\theta [S_{lm}(\theta, \omega)]^2 \sin \theta = \frac{1}{2\pi}. \quad (3.7)$$

The choice of normalization is arbitrary in the sense that it does not change any physical predictions. However, in order to compare equations from other papers in which a different convention was used, we must state our choice explicitly. The functions  $S_{lm}(\theta, \omega)$  will be used as a basis to express functions  $f(t, \theta, \phi)$  as follows:

$$f(t, \theta, \phi) = \sum_{l=2}^{\infty} \sum_{m=-l}^l \int_{-\infty}^{\infty} d\omega \langle lm\omega | f \rangle S_{lm}(\theta, \omega) e^{-i\omega t + im\phi}, \quad (3.8)$$

<sup>9</sup> Although not stated there, this is the normalization convention used in Ref. [1].

where

$$\langle lm\omega|f\rangle = \frac{1}{2\pi} \int dt \int d\Omega f(t, \theta, \phi) S_{lm}(\theta, \omega) e^{i\omega t - im\phi}, \quad (3.9)$$

so that we have  $\langle l'm'\omega'|lm\omega\rangle = \delta_{ll'}\delta_{mm'}\delta(\omega - \omega')$ .

We now return to the case where the source  $\mathcal{J}$  in the master equation (3.2) is nonvanishing. Assuming a solution of the form

$$\varphi = \rho^{-4}\psi_4 = \sum_{l=2}^{\infty} \sum_{m=-l}^l \int d\omega \varphi_{lm}(\omega), \quad (3.10)$$

where

$$\varphi_{lm}(\omega) = R_{lm}(r, \omega) S_{lm}(\theta, \omega) e^{-i\omega t + im\phi}, \quad (3.11)$$

implies that the radial function  $R_{lm}(r, \omega)$  must satisfy

$$\left[ \Delta^2 \frac{d}{dr} \left( \frac{1}{\Delta} \frac{d}{dr} \right) - \mathcal{V}_{lm}(r, \omega) \right] R_{lm}(r, \omega) = -\mathcal{J}_{lm}(r, \omega), \quad (3.12)$$

where  $\mathcal{J}_{lm}(r, \omega) = \langle lm\omega|\mathcal{J}\rangle$ , and the potential is given by

$$\mathcal{V}_{lm}(r, \omega) = -\frac{K^2 + 4i(r-M)K}{\Delta} + 8i\omega r + \lambda_{lm}(\omega). \quad (3.13)$$

Here  $K = (r^2 + a^2)\omega - ma$ , and

$$\lambda_{lm}(\omega) = -C_{lm}(\omega) - 2am\omega. \quad (3.14)$$

The radial equation (3.5a) is just the source free (homogeneous) version of the previous radial equation (3.12). The two independent solutions to the homogeneous radial equation will be used to construct the solution to the inhomogeneous equation. We use the so-called ‘‘in-up basis’’  $\{R_{lm}^H(r, \omega), R_{lm}^\infty(r, \omega)\}$ , which is defined by the following limiting behavior [7]:

$$R_{lm}^H(r \rightarrow r_+, \omega) = B_{lm}^{\text{hole}}(\omega) \Delta^2 e^{-iPr^*}, \quad (3.15a)$$

$$R_{lm}^H(r \rightarrow \infty, \omega) = B_{lm}^{\text{out}}(\omega) r^3 e^{i\omega r^*} + \frac{B_{lm}^{\text{in}}(\omega)}{r} e^{-i\omega r^*}, \quad (3.15b)$$

$$R_{lm}^\infty(r \rightarrow r_+, \omega) = D_{lm}^{\text{out}}(\omega) e^{iPr^*} + D_{lm}^{\text{in}}(\omega) \Delta^2 e^{-iPr^*}, \quad (3.15c)$$

$$R_{lm}^\infty(r \rightarrow \infty, \omega) = D_{lm}^\infty(\omega) r^3 e^{i\omega r^*}. \quad (3.15d)$$

Here  $P = \omega - ma/(2Mr_+)$ , and the ‘‘tortoise coordinate’’  $r^*$  satisfies  $dr^*/dr = (r^2 + a^2)/\Delta$ :

$$r^*(r) = r + \frac{2Mr_+}{r_+ - r_-} \ln \frac{r - r_+}{2M} - \frac{2Mr_-}{r_+ - r_-} \ln \frac{r - r_-}{2M}, \quad (3.16)$$

where  $r_\pm = M \pm \sqrt{M^2 - a^2}$  are the roots of  $\Delta$  ( $r = r_+$  is the location of the event horizon).

The numerical calculation of the homogeneous solutions, say  $R_{lm}^H(r)$ , would in principle work as follows.

First set  $B_{lm}^{\text{in}}(\omega) = 1$  (a normalization convention). Then note that

$$\frac{R_{lm}^H(r \rightarrow r_+)}{B_{lm}^{\text{hole}}(\omega)} = \Delta^2 e^{-iPr^*}, \quad (3.17)$$

$$\frac{R_{lm}^H(r \rightarrow \infty)}{B_{lm}^{\text{hole}}(\omega)} = \frac{B_{lm}^{\text{out}}(\omega)}{B_{lm}^{\text{hole}}(\omega)} r^3 e^{i\omega r^*} + \frac{1}{B_{lm}^{\text{hole}}(\omega) r} e^{-i\omega r^*}. \quad (3.18)$$

Next starting near the horizon at  $r = r_+$ , integrate forward. When we reach  $r \approx \infty$ , we can read off  $B^{\text{out}}/B^{\text{hole}}$  and  $1/B^{\text{hole}}$ . (When clarity permits, we will often drop the somewhat cumbersome subscripts  $l, m$  and the dependence on  $r, \omega$ .) Since the first term in Eq. (3.18) grows rapidly with  $r$ , the two terms cannot be extracted with equal accuracy. We work around this by instead solving the homogeneous Sasaki-Nakamura equation [46] (which was designed to avoid this problem) and converting the result to  $R^{H, \infty}$ ; see Ref. [1] for details. Recently Fujita and Tagoshi have worked out a sophisticated numerical scheme for computing the functions  $R^{H, \infty}$  numerically with great accuracy (with fractional accuracies  $\sim 10^{-14}$  in the corresponding energy fluxes for orbits which are both circular and equatorial) [54].

The general solution to the radial equation (3.12), corresponding to the retarded solution of the master equation (3.2), is

$$R_{lm}(r, \omega) = Z_{lm}^H(r, \omega) R_{lm}^\infty(r, \omega) + Z_{lm}^\infty(r, \omega) R_{lm}^H(r, \omega), \quad (3.19)$$

where the functions  $Z$  are radial integrals over the source term:

$$Z_{lm}^H(r, \omega) = -\frac{1}{\mathcal{A}_{lm}(\omega)} \int_{r_+}^r dr' \frac{R_{lm}^H(r', \omega)}{\Delta'^2} \mathcal{J}_{lm}(r', \omega), \quad (3.20a)$$

$$Z_{lm}^\infty(r, \omega) = -\frac{1}{\mathcal{A}_{lm}(\omega)} \int_r^\infty dr' \frac{R_{lm}^\infty(r', \omega)}{\Delta'^2} \mathcal{J}_{lm}(r', \omega). \quad (3.20b)$$

The function  $\mathcal{A}_{lm}(\omega)$  is given by<sup>10</sup>

$$\mathcal{A}_{lm}(\omega) = 2i\omega B_{lm}^{\text{in}}(\omega) D_{lm}^\infty(\omega). \quad (3.21)$$

This construction of  $Z^{H, \infty}$  and  $\mathcal{A}$  follows from the theory of Green’s functions [55].

In this paper, we only evaluate the perturbed field  $\psi_4$  [and therefore the functions  $Z$  (3.20)] outside the orbital torus —  $r < r_{\text{min}}$  and  $r > r_{\text{max}}$ . Evaluating  $\psi_4$  at arbitrary locations within the orbital torus  $r_{\text{min}} < r < r_{\text{max}}$  would require a more complicated numerical apparatus than the one developed here.

<sup>10</sup> The value of  $\mathcal{A}$  reported in Ref. [1] has the wrong sign.

## B. Bound test mass sources

Beginning from Teukolsky's original expression for the source term  $\mathcal{T}$  [22], Breuer [56] has computed the explicit form of the projected source (see Ref. [57] or Sec. IV C of Ref. [1]):

$$\mathcal{T}_{lm}(r, \omega) = \int d\Omega dt \mathcal{B}_m(t, r, \theta, \phi, \omega) S_{lm}(\theta, \omega) e^{i\omega t - im\phi}, \quad (3.22)$$

where

$$\begin{aligned} \mathcal{B}_m = & \sqrt{2}\Delta^2 \rho^3 L_{-1}[\rho^{-4} \bar{\rho}^2 J_+(\rho^{-2} \bar{\rho}^{-2} \Delta^{-1} T_{n\bar{m}})] \\ & - 2\rho^3 L_{-1}[\rho^{-4} L_0(\rho^{-2} \bar{\rho}^{-1} T_{nn})] \\ & + \sqrt{2}\Delta^2 \rho^3 J_+[\rho^{-4} \bar{\rho}^2 \Delta^{-1} L_{-1}(\rho^{-2} \bar{\rho}^{-2} T_{n\bar{m}})] \\ & - \Delta^2 \rho^3 J_+[\rho^{-4} J_+(\rho^{-2} \bar{\rho} T_{\bar{m}\bar{m}})]. \end{aligned} \quad (3.23)$$

This function is given in terms of the tetrad components of the orbiting particle's energy-momentum tensor,

$$T_{ab} = T^{\alpha\beta} a_\alpha b_\beta, \quad (3.24)$$

where  $T^{\alpha\beta}$  is the energy-momentum tensor of the particle, and  $a$  and  $b$  are either  $n$  or  $\bar{m}$ . We define the derivative operators

$$J_+ = \partial_r + iK/\Delta \quad (3.25)$$

$$L_s = \partial_\theta + m \csc \theta - a\omega \sin \theta + s \cot \theta. \quad (3.26)$$

In Kerr spacetime, a point particle of mass  $\mu$  has an energy-momentum tensor given by

$$T^{\alpha\beta}(t, r, \theta, \phi) = \frac{\mu u^\alpha u^\beta d\tau}{\Sigma \sin \theta} \delta[r - r(t)] \delta[\theta - \theta(t)] \delta[\phi - \phi(t)], \quad (3.27)$$

where  $u^\alpha$  is the particle's 4-velocity. The quantities  $r(t)$ ,  $\theta(t)$ , and  $\phi(t)$  appearing in Eq. (3.27) are the coordinates of the geodesic at coordinate time  $t$ , and should not be confused with  $r$ ,  $\theta$ , and  $\phi$  in the definition of the source term (3.22).

We use the Newman-Penrose basis given by Kinnersly [58] [see Eqs. (B2) and (B3)]. This means the tetrad components of  $T^{\alpha\beta}$  are given by

$$T_{ab} = \frac{C_{ab}}{\sin \theta} \delta[r - r(t)] \delta[\theta - \theta(t)] \delta[\phi - \phi(t)], \quad (3.28)$$

where<sup>11</sup> [57]

$$C_{nn} = \frac{d\lambda}{dt} \frac{\mu}{4\Sigma^2} \left[ E(r^2 + a^2) - aL_z + \frac{dr}{d\lambda} \right]^2, \quad (3.29a)$$

$$C_{\bar{m}\bar{m}} = \frac{d\lambda}{dt} \frac{\mu \rho^2}{2} \left[ i \left( aE - \frac{L_z}{\sin^2 \theta} \right) \sin \theta + \frac{d\theta}{d\lambda} \right]^2, \quad (3.29b)$$

$$\begin{aligned} C_{n\bar{m}} = & \frac{d\lambda}{dt} \frac{\mu \rho}{2\sqrt{2}\Sigma} \left[ E(r^2 + a^2) - aL_z + \frac{dr}{d\lambda} \right] \\ & \times \left[ i \left( aE - \frac{L_z}{\sin^2 \theta} \right) \sin \theta + \frac{d\theta}{d\lambda} \right]. \end{aligned} \quad (3.29c)$$

These functions (3.29) depend explicitly on  $dr/d\lambda$  and  $d\theta/d\lambda$ , rather than on their squares  $V_{r,\theta}$ . Extra book-keeping is thus needed to keep track of the signs of  $dr/d\lambda$  and  $d\theta/d\lambda$  when evaluating them numerically.

Following the details shown in (for example) Ref. [1], we can now write the projected source term (3.22) in the following form

$$\begin{aligned} \mathcal{T}_{lm}(r, \omega) = & \int dt \Delta^2 \{ [A_{nn0} + A_{n\bar{m}0} + A_{\bar{m}\bar{m}0}] \delta[r - r(t)] \\ & + \partial_r [(A_{n\bar{m}1} + A_{\bar{m}\bar{m}1}) \delta(r - r\{t\})] \\ & + \partial_r^2 [A_{\bar{m}\bar{m}2} \delta(r - r\{t\})] \} e^{i\omega t - im\phi(t)}. \end{aligned} \quad (3.30)$$

The quantities  $A_{abc}$  are shown explicitly in Appendix B.

Substituting Eq. (3.30) into Eq. (3.20) and eliminating the radial delta functions gives

$$\begin{aligned} Z_{lm}^*(r, \omega) = & -\frac{1}{A} \int dt e^{i\omega t - im\phi(t)} \Theta^*[r, r(t)] \\ & [(A_{nn0} + A_{n\bar{m}0} + A_{\bar{m}\bar{m}0}) \\ & - (A_{n\bar{m}1} + A_{\bar{m}\bar{m}1}) \frac{d}{dr} + A_{\bar{m}\bar{m}2} \frac{d^2}{dr^2}] R_{lm}^*, \end{aligned} \quad (3.31)$$

where  $\star = \text{H}, \infty$ . We define the step functions

$$\Theta^\infty(x_1, x_2) = \Theta^{\text{H}}(x_2, x_1) = \Theta(x_2 - x_1), \quad (3.32)$$

in terms of the Heaviside step function  $\Theta(x)$ . All other functions of  $r$  and  $\theta$  under the integral in Eq. (3.31) are to be evaluated at  $r(t)$  and  $\theta(t)$  respectively. Because  $r$  only appears inside the step functions, the quantities  $Z^{\text{H}, \infty}$  are independent of  $r$  for all  $r > r_{\text{max}}$  and  $r < r_{\text{min}}$ .

To clean up this expression, we now absorb most of the integrand into a single function:

$$Z_{lm}^*(r, \omega) = \int dt e^{i\omega t - im\phi(t)} I_{lm}^*(t, r, \omega). \quad (3.33)$$

<sup>11</sup> In Ref. [59], the  $d\theta/d\tau$  terms are missing from the expressions for  $C_{n\bar{m}}$  and  $C_{\bar{m}\bar{m}}$ . Also, in Ref. [2]  $d\theta/d\lambda$  is erroneously replaced with  $(d\theta/d\lambda)^2$ .

Following the arguments in Sec. V B of Ref. [44], we exploit the harmonic structure of the geodesics (Sec. II) to simplify Eq. (3.33). In the end, we will arrive at a general expression for  $\psi_4$  (3.10) as a discrete sum over frequencies, rather than an integral. First we insert

$$t = \Gamma\lambda + \Delta t, \quad \phi = \Upsilon_\phi\lambda + \Delta\phi, \quad (3.34)$$

into Eq. (3.33), and we change the integration variable from  $t$  to  $\lambda$ . The result is

$$Z_{lm}^*(r, \omega) = \int d\lambda e^{i(\omega\Gamma - m\Upsilon_\phi)\lambda} J_{lm}^*(\lambda, r, \omega), \quad (3.35)$$

where

$$J_{lm}^*(\lambda, r, \omega) = \frac{dt}{d\lambda} e^{i\omega\Delta t - im\Delta\phi} I_{lm}^*(\lambda, r, \omega). \quad (3.36)$$

The function  $J_{lm}^*(\lambda, r, \omega)$  is biperiodic, so we can write it as [44]

$$J_{lm}^*(\lambda, r, \omega) = \sum_{kn} J_{lmkn}^* e^{-i(k\Upsilon_\theta + n\Upsilon_r)\lambda}; \quad (3.37)$$

the constants  $J_{lmkn}^*$  are given by

$$J_{lmkn}^* = \frac{1}{(2\pi)^2} \int_0^{2\pi} d w_\theta \int_0^{2\pi} d w_r e^{i(k w_\theta + n w_r)} \times J_{lm}^*[r(w_r), \theta(w_\theta), r, \omega]. \quad (3.38)$$

By inserting the expansion (3.37) into Eq. (3.35), we find that the integral (3.35) is just a sum of delta functions:

$$Z_{lm}^*(r, \omega) = \sum_{kn} Z_{lmkn}^*(r) \delta(\omega - \omega_{mkn}). \quad (3.39)$$

We have used the coordinate time frequencies (2.20) to define

$$\omega_{mkn} = m\Omega_\phi + k\Omega_\theta + n\Omega_r. \quad (3.40)$$

The expansion coefficients for  $Z_{lm}^*(r, \omega)$  are given by

$$Z_{lmkn}^*(r) = \frac{1}{2\pi\Gamma} \int_0^{2\pi} d w_\theta \int_0^{2\pi} d w_r e^{i k w_\theta + i n w_r} \times J_{lm}^*(w_r, w_\theta, r, \omega_{mkn}), \quad (3.41)$$

By substituting the expanded form (3.39) of  $Z$  into the general expression (3.10) for  $\psi_4$ , we eliminate the frequency integral to obtain

$$\psi_4 = \rho^4 \sum_{lmkn} R_{lmkn}(r) S_{lmkn}(\theta) e^{-i\omega_{mkn}t + im\phi}. \quad (3.42)$$

The radial and angular functions are now discrete functions of frequency, inheriting the angular harmonic index  $k$  and the radial harmonic index  $n$ :

$$S_{lmkn}(\theta) = S_{lm}(\theta, \omega_{mkn}), \quad (3.43)$$

$$R_{lmkn}^*(r) = R_{lm}^*(r, \omega_{mkn}), \quad (3.44)$$

$$R_{lmkn}(r) = Z_{lmkn}^H(r) R_{lmkn}^\infty(r) + Z_{lmkn}^\infty(r) R_{lmkn}^H(r). \quad (3.45)$$

### C. Numerical considerations

Because the functions  $r(w_r)$  and  $\theta(w_\theta)$  are periodic and even [cf. Eq. (2.12)], the range of the integrals (3.41) can be reduced by a factor of two. Writing the integrand in (3.41) as  $z(w_r, w_\theta)$ , we can expand the integrals into the form

$$Z = \left[ \int_0^\pi d w_\theta \int_0^\pi d w_r + \int_0^\pi d w_\theta \int_\pi^{2\pi} d w_r + \int_\pi^{2\pi} d w_\theta \int_0^\pi d w_r + \int_\pi^{2\pi} d w_\theta \int_\pi^{2\pi} d w_r \right] z(w_r, w_\theta). \quad (3.46)$$

Since the integrand has a period of  $2\pi$  in both variables, we can shift all of the  $\{\pi, 2\pi\}$  branches to  $\{-\pi, 0\}$ :

$$Z = \left[ \int_0^\pi d w_\theta \int_0^\pi d w_r + \int_0^\pi d w_\theta \int_{-\pi}^0 d w_r + \int_{-\pi}^0 d w_\theta \int_0^\pi d w_r + \int_{-\pi}^0 d w_\theta \int_{-\pi}^0 d w_r \right] z(w_r, w_\theta). \quad (3.47)$$

We can now reflect all of the  $\{-\pi, 0\}$  branches across the origin to get

$$Z = \int_0^\pi d w_\theta \int_0^\pi d w_r \sum_{D_r=\pm} \sum_{D_\theta=\pm} z(D_r w_r, D_\theta w_\theta). \quad (3.48)$$

Direct evaluation of Eq. (3.48) is complicated by the fact that it is difficult to evaluate  $r(w_r)$  and  $\theta(w_\theta)$  [see discussion preceding Eq. (2.27)]. We avoid this problem by changing integration variables from  $w_r$  and  $w_\theta$  to  $\psi$  and  $\chi$  [see Eq. (2.26)].

Eccentric orbits introduce another numerical nuance. The integrand in Eq. (3.48) is moderately divergent if the orbit covers a large range in  $r$  (i.e., if the orbit is highly eccentric). This problem can be traced to the scaling behavior (3.15) of solutions to the homogeneous radial equation. In particular, the typical size of the integrand at  $r_{\min}$  can be different from typical values at  $r_{\max}$  by orders of magnitude. This causes an artificial focusing of numerical accuracy. Our choice of boundary conditions (2.11) is such that the turning points  $r_{\min}$  and  $r_{\max}$  occur at  $\psi = 0$  and  $\psi = \pi$  respectively. To avoid this problem, we introduce a change of integration variables from  $\psi$  to  $\zeta$  where  $d\psi/d\zeta = e^{-\psi/\Psi^*}$ , with  $\star = H, \infty$ , and

$$\zeta(\psi) = \Psi^* \left( e^{\psi/\Psi^*} - 1 \right). \quad (3.49)$$

Here  $\Psi^*$  is a constant (which can be positive or negative). Before integrating, we tune the value of  $\Psi^*$  so that the typical magnitude of the integrand at the outer turning point is comparable to that at the inner turning point. In general, the value of  $\Psi^*$  will decrease if either  $l$  or eccentricity  $e$  are increased.

Applying these various changes of variable and massaging of the integration ranges to Eq. (3.41), our final expression for the  $Z_{lmkn}^*(r)$  coefficients is given by

$$\begin{aligned} Z_{lmkn}^*(r) = & \frac{1}{2\pi\Gamma} \int_0^\pi d\chi \int_0^{\zeta(\pi)} d\zeta \sum_{D_r=\pm} \sum_{D_\theta=\pm} \frac{dw_\theta}{d\chi} \frac{dw_r}{d\psi} \frac{dt}{d\lambda} \\ & \times e^{-\psi/\Psi^*} I_{lm}^*(w_r, w_\theta, D_r, D_\theta, r, \omega_{mkn}) \\ & \times \exp [iD_\theta (kw_\theta + \omega_{mkn}\Delta t^\theta - m\Delta\phi^\theta)] \\ & \times \exp [iD_r (nw_r + \omega_{mkn}\Delta t^r - m\Delta\phi^r)], \end{aligned} \quad (3.50)$$

where  $I_{lm}^*$  is defined by Eq. (3.33). The functions  $r(t)$ ,  $\theta(t)$  and their derivatives are evaluated as

$$\begin{aligned} r(t) \rightarrow r(\zeta), \quad \frac{dr}{d\lambda}[r(t)] & \rightarrow D_r \left| \frac{dr}{d\lambda}[r(\zeta)] \right|, \\ \theta(t) \rightarrow \theta(\chi), \quad \frac{d\theta}{d\lambda}[\theta(t)] & \rightarrow D_\theta \left| \frac{d\theta}{d\lambda}[\theta(\chi)] \right|. \end{aligned} \quad (3.51)$$

Lastly, note that applying the simultaneous transformations  $m \rightarrow -m$ ,  $\omega \rightarrow -\omega$  to the radial (3.12) and the angular equations (3.5b), one can derive a simple symmetry rule for expansion coefficients [1, 2]

$$Z_{l(-m)(-k)(-n)}^*(r) = (-1)^{l+k} \bar{Z}_{lmkn}^*(r). \quad (3.52)$$

This symmetry is used to reduce the computation time for various summations (see Sec. IV C).

#### D. Waveforms and fluxes

In this section, we use the expanded form of the curvature perturbation (3.42) to derive expressions for the leading order metric perturbation at infinity, and for the radiated fluxes of energy and angular momentum to infinity and down the black hole's event horizon. Since we will be interested in quantities at both infinity and the horizon, it will be useful to first define the limiting values of the coefficients  $Z_{lmkn}^*(r)$  as follows:

$$Z_{lmkn}^H = D_{lmkn}^\infty Z_{lmkn}^H(r > r_{\max}), \quad (3.53a)$$

$$Z_{lmkn}^\infty = B_{lmkn}^{\text{hole}} Z_{lmkn}^\infty(r < r_{\min}). \quad (3.53b)$$

Recall that the functions  $Z_{lmkn}^*(r)$  are independent of  $r$  for all  $r > r_{\max}$  and  $r < r_{\min}$ .

At infinity, the leading order curvature and metric perturbations are related by

$$\psi_4(r \rightarrow \infty) = \frac{1}{2} \frac{\partial^2}{\partial t^2} (h_+ - ih_\times). \quad (3.54)$$

Here  $h_+$  and  $h_\times$  are the two independent components of the metric perturbation, defined by

$$h_{\alpha\beta}(r \rightarrow \infty) = h_+ e_{\alpha\beta}^+ + h_\times e_{\alpha\beta}^\times + O(1/r^2), \quad (3.55)$$

where  $e_{\alpha\beta}^+$  and  $e_{\alpha\beta}^\times$  are polarization tensors [60]. If we now substitute the expanded form of the curvature perturbation (3.42) into the left hand side of Eq. (3.54), evaluate the limit, and integrate twice in coordinate time (setting the arbitrary integration constants to zero), we find

$$h_+ - ih_\times = -\frac{2}{r} \sum_{lmkn} \frac{Z_{lmkn}^H}{\omega_{mkn}^2} S_{lmkn}(\theta) e^{-i\omega_{mkn}(t-r) + im\phi}. \quad (3.56)$$

We have used the definition (3.53a) for the limiting value of  $Z_{lmkn}^H(r)$ .

It is important to note that the expression for  $Z_{lmkn}^H$  derived above [e.g. Eq. (3.50)] assumed geodesics with a specific choice of initial position:  $r(0) = r_{\min}$ ,  $\theta(0) = \theta_{\min}$ ,  $t(0) = 0$ , and  $\phi(0) = 0$ . These are the fiducial geodesics from Ref. [7]. Making a different choice of initial position will result in an overall phase change for  $Z_{lmkn}^H$ . The details of this phase can be found in Ref. [7]. As we will see below, the expression for the waveform (3.56) is unique in that, unlike the formulas for evolving  $E$ ,  $L_z$ , it depends explicitly on this overall phase, and therefore on the initial position of the geodesic.

At infinity, the effective energy-momentum tensor  $T_{\alpha\beta}^{\text{GW}}$  is easily built from the GWs [61]. The result can be expressed as [60]

$$T_{\alpha\beta}^{\text{GW}} = \frac{1}{16\pi} \left\langle \frac{\partial h_+}{\partial x^\alpha} \frac{\partial h_+}{\partial x^\beta} + \frac{\partial h_\times}{\partial x^\alpha} \frac{\partial h_\times}{\partial x^\beta} \right\rangle. \quad (3.57)$$

Brackets indicate an average over several wavelengths of the gravitational waves. Using this result and the expansion (3.56), it is straightforward to show that waves carry an averaged flux of energy and angular momentum given by

$$\left\langle \frac{dE}{dt} \right\rangle^\infty = \sum_{lmkn} \frac{1}{4\pi\omega_{mkn}^2} |Z_{lmkn}^H|^2, \quad (3.58a)$$

$$\left\langle \frac{dL_z}{dt} \right\rangle^\infty = \sum_{lmkn} \frac{m}{4\pi\omega_{mkn}^3} |Z_{lmkn}^H|^2. \quad (3.58b)$$

Similar expressions can be found for the flux of energy and angular momentum through the horizon; we refer the reader to Refs. [1, 52, 62] for a detailed derivation. The resulting fluxes are

$$\left\langle \frac{dE}{dt} \right\rangle^H = \sum_{lmkn} \frac{1}{4\pi\omega_{mkn}^2} \alpha_{lmkn} |Z_{lmkn}^\infty|^2, \quad (3.59a)$$

$$\left\langle \frac{dL_z}{dt} \right\rangle^H = \sum_{lmkn} \frac{m}{4\pi\omega_{mkn}^3} \alpha_{lmkn} |Z_{lmkn}^\infty|^2. \quad (3.59b)$$

The superscripts we use here are somewhat confusing: the fluxes to infinity depend upon the *horizon* coefficients,  $Z_{lmkn}^H$ , and the fluxes down the horizon depend upon the *infinity* coefficients  $Z_{lmkn}^\infty$ . This seemingly obtuse convention comes from the Green's function solution

we constructed, Eq. (3.45). The coefficients  $Z^H$  set the amplitude of the radial behavior towards infinity; the coefficients  $Z^\infty$  set the amplitude towards the horizon.

The coefficient  $\alpha_{lmkn}$  appearing in Eq. (3.59) is given by [1]

$$\alpha_{lmkn} = \frac{256(2Mr_+)^5 P(P^2 + 4\epsilon^2)(P^2 + 16\epsilon^2)\omega_{mkn}^3}{|C_{lmkn}|^2}, \quad (3.60)$$

with  $\epsilon = \sqrt{M^2 - a^2}/4Mr_+$ , where  $r_+$  is the location of the event horizon, and

$$\begin{aligned} |C_{lmkn}|^2 &= [(\lambda_{lmkn} + 2)^2 + 4a\omega_{mkn} - 4a^2\omega_{mkn}^2] \\ &\times (\lambda_{lmkn}^2 + 36ma\omega_{mkn} - 36a^2\omega_{mkn}^2) \\ &+ (2\lambda_{lmkn} + 3)(96a^2\omega_{mkn}^2 - 48ma\omega_{mkn}) \\ &+ 144\omega_{mkn}^2(M^2 - a^2). \end{aligned} \quad (3.61)$$

Recall that  $P = \omega_{mkn} - ma/(2Mr_+)$ , and that  $\lambda_{lmkn}$  is related to angular equation's eigenvalue [cf. Eq. (3.5b)] via Eq. (3.14) with  $\omega = \omega_{mkn}$ .

To go from snapshot waveforms to adiabatic inspiral waveforms, we must evolve not just energy and angular momentum, but also the Carter constant  $Q$ . This will eventually be done with the formalism recently derived by Mino [5]. However, if we assume that radiation does not influence an orbit's inclination [ $\iota$  or equivalently  $\theta_{\text{inc}}$ ], we can infer an expression for  $\langle dQ/dt \rangle$ . This scheme was first suggested by Curt Cutler [63]. From the definition (2.7) of  $\iota$ , we see that setting  $\langle d\iota/dt \rangle = 0$  gives

$$\left\langle \frac{dQ}{dt} \right\rangle = \frac{2Q}{L_z} \left\langle \frac{dL_z}{dt} \right\rangle, \quad (3.62)$$

where  $\langle dL_z/dt \rangle = \langle dL_z/dt \rangle^H + \langle dL_z/dt \rangle^\infty$ . Hughes showed that this approximation is reasonable in the case of circular orbits [36]. It is currently unknown how accurate it may be in the case of generic orbits (though it is almost certainly *pathological* for orbits with nearly vanishing  $L_z$  [64]). In Sec. V below, we report values of  $\langle dQ/dt \rangle$  given by Eq. (3.62). We should emphasize however that, since Eq. (3.62) is itself a speculation, those results will very likely be less accurate than the associated fluxes of energy and angular momentum.

#### IV. NUMERICAL ALGORITHM

For a given orbit, the calculation of the snapshot waveform is essentially identical to the calculation of each of the radiative fluxes. Given an engine which can compute the  $Z_{lmkn}^*$  coefficients, which we will refer to simply as modes, each calculation is essentially just a long four dimensional summation. In the following three subsections, we describe the details of our algorithms for (i) computing the frequency domain representations of the geodesics, (ii) computing the individual modes  $Z_{lmkn}^*$ , and (iii) truncating the sums representing the waveforms and fluxes.

#### A. Geodesics

We begin by computing the quantities associated with the specified geodesic for a given set of black hole and orbital parameters  $(a, e, p, \theta_{\text{inc}})$ . This calculation proceeds as follows:

1. Compute the constants of the motion  $E, L_z, Q$
2. Compute the orbital frequencies  $\Upsilon_{r,\theta,\phi}$ , and  $\Gamma$
3. Construct routines to evaluate  $w_r(\psi), w_\theta(\chi)$  and their derivatives
4. Construct the expansions (2.23a) of  $\Delta t$  and  $\Delta\phi$

Explicit expressions for the first three of these steps are shown in Appendix A. The last step requires that we approximate the sums for the expansions (2.23a) of  $\Delta x = \Delta t, \Delta\phi$  as

$$\Delta x^\theta \approx \sum_{k=1}^K \Delta x_k^\theta \sin(kw_\theta), \quad \Delta x^r \approx \sum_{n=1}^N \Delta x_n^r \sin(nw_r), \quad (4.1)$$

where we determine the values of  $K$  and  $N$  by requiring that 15 consecutive  $\Delta x_{k,n}^{r,\theta}$  coefficients make fractional contributions to the sum which are less than some specified accuracy; we typically find  $K, N \lesssim 50$ . Each of these calculations associated with the geodesics is done to a fractional accuracy of  $10^{-12}$ , and the results are made available to the remaining computations. The calculations described so far are typically completed in a few seconds (using a single  $\sim 1$  GHz processor). It's worth bearing in mind that these calculations need only be done once when computing the waveform and fluxes for a given orbit.

#### B. Modes

After computing geodesic quantities, we construct an engine for calculating the modes  $Z_{lmkn}^*$ . This requires solutions to the angular equation, and to the homogeneous radial equation. (Our homogeneous solutions have an implicit coupling to the source, since they depend on the frequencies  $\omega_{mkn}$ , which are determined by the orbit.) The routines for solving the homogeneous radial and angular equations were inherited from the code used in Ref. [1], where they are described in detail. We solve the angular equation to nearly machine accuracy, and we solve the radial equation to a fractional accuracy of  $\min(10^{-7}, \varepsilon_{\text{flux}}/100)$ , where  $\varepsilon_{\text{flux}}$  is the overall fractional accuracy demanded of the waveforms and fluxes.

When computing (3.50), we treat the radial integral as the outermost integral [the reverse of how we have written Eq. (3.50)]. After experimenting with a variety of numerical methods for evaluating these integrals, we found a Clenshaw-Curtis quadrature algorithm to be the most

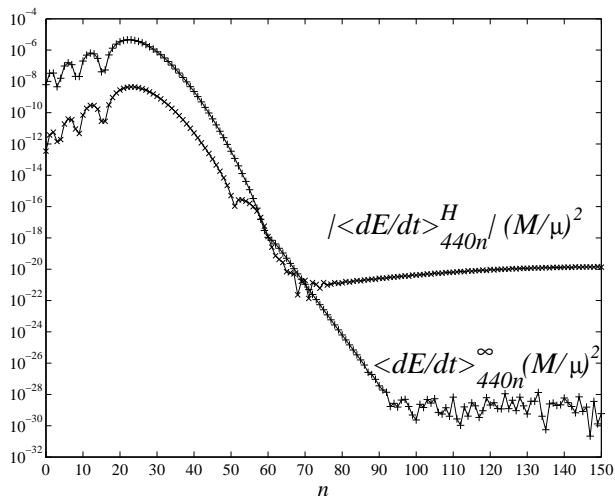


FIG. 2: Modal energy flux through the horizon (superscript H, marked with  $\times$ 's) and at radial infinity (superscript  $\infty$ , marked with  $+$ 's). Results are for  $l = m = 4$ ,  $k = 0$ . The orbit has eccentricity  $e = 0.7$ , inclination  $\theta_{\text{inc}} = 45^\circ$ , and semilatus rectum  $p = 5.1$ , while the massive black hole has  $a = 0.9M$ .

efficient. This method analytically integrates a numerical series representation (in Chebyshev polynomials) of the integrand, to produce a series representation of the integral (for more details, see for example Ref. [65]). Each of these calculations depends on the indices  $(l, m, k, n)$ , and must be repeated many times to compute the waveform and fluxes associated with a given orbit.

We compute the angular integral in Eq. (3.50) to a fractional accuracy of  $\min(10^{-6}, \varepsilon_{\text{flux}}/10)$ . The accuracy demanded of the radial integral is chosen dynamically. We begin by asking for a fractional accuracy of  $\min(10^{-5}, \varepsilon_{\text{flux}})$ . As each mode is computed, we store the magnitude of the largest modes encountered so far. Later modes are then computed to a fractional accuracy of at least 10%. After this 10% accuracy has been achieved the integrator continues to add more terms to the Chebyshev expansion. At each iteration it estimates the associated uncertainty in the total energy fluxes (the energy flux at the horizon for the  $Z_{lmkn}^\infty$  integrals, and the energy flux at infinity for the  $Z_{lmkn}^H$  integrals) by comparing to the magnitudes of the largest known modes. It then truncates the Chebyshev expansion as soon as the integral's associated relative flux error is smaller than  $\varepsilon_{\text{flux}}$ . The reason for this dynamic accuracy control is that many of the modes are very near zero. If we know that the total flux contains modes which are  $\sim 10^{-3}$ , there is no need to compute a mode which is  $\sim 10^{-20}$  beyond the first couple of digits. A single  $\sim 1$  GHz processor usually takes considerably less than a second to compute both  $Z_{lmkn}^\infty$  and  $Z_{lmkn}^H$  (see Fig. 1 in Ref. [6]), unless the modes are especially badly behaved in the sense described in Sec. IV C below. In these rare cases the modes can take anywhere from 10 seconds to a minute to compute.

When computing a flux, the majority of the numerical work is devoted to computing modes which are insignificant or zero. The integrator has little difficulty when computing the dominant modes. However, modes which are very near zero (near round off error) can cause the integrator to fail. This typically happens when computing modes with “large” values of the indices  $(l, m, k, n)$ ; the meaning of “large” is somewhat orbit and index dependent. For example, for fixed  $(l, m, k)$ , we find that there is some limiting value of  $n$  beyond which the mode calculations cannot be trusted.

We show an example of this behavior in Fig. 2. Beyond the dominant modes at  $n \simeq 20$ , the mode magnitudes fall (roughly) exponentially until reaching a bottom. For the case shown in Fig. 2, the horizon modes bottom out at about  $n = 70$ , after which they gradually diverge, while the infinity modes bottom out at about  $n = 90$ , after which they appear to be dominated by numerical error. Both behaviors are unphysical since they indicate a divergent total energy flux. The different behaviors arise from the different scalings of these modes with frequency:

$$\left\langle \frac{dE}{dt} \right\rangle_{lmkn}^\infty \sim \omega_{mkn}^{-2} |Z_{lmkn}^H|^2, \quad (4.2)$$

$$\left\langle \frac{dE}{dt} \right\rangle_{lmkn}^H \sim \omega_{mkn}^2 |Z_{lmkn}^\infty|^2. \quad (4.3)$$

This difference comes from the factor  $\alpha_{lmkn} \sim \omega_{mkn}^4$  in Eq. (3.59).

For reasonable requested accuracies, the modes which are difficult to compute are always insignificant when compared to the dominant modes (as is clearly the case in Fig. 2). In the vast majority of cases, the truncation rules (see Sec. IV C below) have been invoked long before these badly behaved modes are encountered. If this is not the case, these badly behaved modes can undermine the truncation scheme since, despite their small magnitudes, they do not regularly decay with increasing index. In order to account for this, we artificially zero any modes for which the ratio of the magnitude of the integral  $Z_{lmkn}^*$  to the maximum over  $\zeta$  and  $\chi$  of the absolute value of the integrand in Eq. (3.50) is below some threshold. We have found that this ratio is a good indicator of when the modes have bottomed out in the sense shown in Fig. 2. Unfortunately, we have had to “hand-tune” this parameter somewhat. This was particularly so as we explored orbits with increasing eccentricity. In the future, we expect to incorporate our code into one which computes inspiral waveforms. Hand tuning of this parameter will be unacceptable for such a code, and a more robust technique will be needed.

### C. Truncation

Given the routines described above, the remaining task is to evaluate the four dimensional sums which make up the waveforms and fluxes (Sec. III D). As mentioned

above, we do this by monitoring the sums which represent the fluxes. We assume that once the fluxes have converged to some requested fractional accuracy  $\varepsilon_{\text{flux}}$ , the sums representing the waveforms are comparably accurate since they are constructed from the same mode coefficients as were used for the fluxes. We now discuss the algorithm for truncating the sums which represent the fluxes.

Let  $F$  be the flux of energy or angular momentum at the horizon or at infinity

$$F = \left\langle \frac{dE}{dt} \right\rangle^{\text{H},\infty}, \quad \left\langle \frac{dL_z}{dt} \right\rangle^{\text{H},\infty}. \quad (4.4)$$

The algorithm for computing these fluxes is:

$$F = \sum_{l=2}^{\infty} F_l, \quad (4.5a)$$

$$F_l = \sum_{m=-l}^l F_{lm}, \quad (4.5b)$$

$$F_{lm} = \sum_{k=-\infty}^{\infty} F_{lmk}, \quad (4.5c)$$

$$F_{lmk} = F_{lmk0} + 2 \sum_{n=1}^{\infty} F_{lmkn}. \quad (4.5d)$$

We have used the symmetry (3.52), which gives

$$F_{lmkn} = F_{l(-m)(-k)(-n)}, \quad (4.6)$$

to simplify the sum over the radial harmonic index  $n$ . Each of the sums which has an infinite boundary is then truncated as described below.

The terms which make up outermost sum,  $F_l$  in the sum over  $l$ , always decrease monotonically with increasing  $l$ . This means that the  $l$ -sum can be written

$$F = \sum_{l=2}^L F_l + \delta F, \quad (4.7)$$

where to a good approximation  $\delta F \approx F_L$ , and  $L$  is a number which is determined by the requested accuracy via

$$|F_L| < \varepsilon_{\text{flux}} \max_l |F_l|. \quad (4.8)$$

The sum over the  $m$ -index is computed for all values  $-l \leq m \leq l$  — we do not truncate it.

The  $k$  and  $n$  sums are approximated as

$$F_{lm} \approx \sum_{k=K_-}^{K_+} F_{lmk}, \quad F_{lmk} \approx F_{lmk0} + 2 \sum_{n=1}^{N_+} F_{lmkn}, \quad (4.9)$$

where the constants  $K_{\pm}$  and  $N_+$  are determined by requiring that the following relation

$$|F_{lmK_{\pm}}| < \varepsilon_{\text{flux}} \max_{l'm'k'} |F_{l'm'k'}|, \quad (4.10a)$$

$$|F_{lmKN_+}| < \varepsilon_{\text{flux}} \max_{l'm'k'n'} |F_{l'm'k'n'}|, \quad (4.10b)$$

(where the maximization is done over all previously encountered mode amplitudes) is satisfied for  $B$  consecutive terms. We also require that the first of these  $B$  terms is larger in magnitude than the last. This extra condition gives some assurance that we are not truncating during a slow rising up of the modes. For the sums over the polar harmonic index  $k$ , we use  $B = 2$ . For the sums over the radial harmonic index  $n$ , we use  $B = 5$  — the dominant radial modes show a less orderly distribution than the polar modes.

The validity of any given truncation scheme is always subject to doubt — it could be the case that modes which haven't been computed are anomalously large in magnitude. In this sense truncating sums can be likened to financial investments: past performance is not necessarily indicative of future results.

We have found these words of caution are especially applicable for the sums over the radial harmonic index  $n$ . We find that the  $F_l$  terms, as defined by Eqs. (4.5), in the outermost sum over  $l$  always decrease monotonically with increasing  $l$ . Also, the  $F_{lmk}$  terms are always peaked near  $k = 0$ , so that setting the buffer  $B$  to a modestly small number is sufficient for catching the dominant modes. Unfortunately, the  $F_{lmkn}$  appear not to obey any similar general rules. If either  $l$  or the eccentricity  $e$  are increased, the  $n$  values of the dominant  $F_{lmkn}$  modes drift to large values of  $n$ . As a result, the truncation rules are expected to be limited in a rough sense by large eccentricity, or by requests for high accuracy (which would require modes with large  $l$ ).

It may be possible to better anticipate  $n$  for the dominant modes. Peters and Mathews [66] used the quadrupole approximation to describe the radiation of two point particles moving along closed Keplerian orbits of arbitrary eccentricity  $e$ . Under this approximation, they decomposed the metric perturbation into tensor spherical harmonics [67] with  $l = 2$ . They then showed that the power  $\langle dE/dt \rangle_n^{\text{PM}}$  radiated at a frequency  $n\omega$  (where  $n$  is an integer and  $\omega$  is the single unique orbital frequency for a Keplerian orbit) is given by

$$\begin{aligned} \left\langle \frac{dE}{dt} \right\rangle_n^{\text{PM}} &\propto \frac{n^4}{32} \left\{ [J_{n-2}(ne) - 2eJ_{n-1}(ne) \right. \\ &\quad \left. + \frac{2}{n}J_n(ne) + 2eJ_{n+1}(ne) - J_{n+2}(ne)]^2 \right. \\ &\quad \left. + (1 - e^2) [J_{n-2}(ne) - 2J_n(ne) + J_{n+2}(ne)]^2 \right. \\ &\quad \left. + \frac{4}{3n^2} [J_n(ne)]^2 \right\}, \quad (4.11) \end{aligned}$$

where  $J_n(x)$  are Bessel functions of the first kind. We have found that this formula (which was derived using only the quadrupole equation and Keplerian orbits) accurately predicts the  $n$  values of the dominant  $F_{lmkn}$  modes for  $l = 2$ . More quantitatively, define  $\tilde{n}$  by

$$\left\langle \frac{dE}{dt} \right\rangle_{\tilde{n}}^{\text{PM}} = \max_n \left\langle \frac{dE}{dt} \right\rangle_n^{\text{PM}}, \quad (4.12)$$

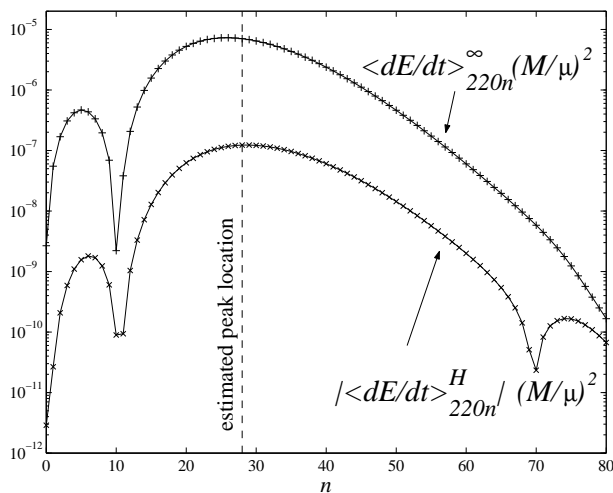


FIG. 3: Modal energy flux through the horizon (superscript H, marked with  $\times$ 's) and at infinity (superscript  $\infty$ , marked with  $+$ 's). The indices  $l = m = 2$ ,  $k = 0$ . The orbit has eccentricity  $e = 0.85$ , inclination  $\theta_{\text{inc}} = 20^\circ$ , and semilatus rectum  $p = 6$ , while the massive black hole has  $a = 0.9M$ . The horizon modes are peaked at  $n = 29$ , while the infinity modes are peaked at  $n = 26$ . The dashed line shows the estimated peak location (at  $n = 28$ ) found using the Peters-Mathews power formula (4.11).

so that

$$\tilde{n} \approx \exp \left[ \frac{1}{2} - \frac{3}{2} \ln(1 - e) \right]; \quad (4.13)$$

this approximate formula was found by fitting to numerically determined maxima of Eq. (4.11). Then, even for highly relativistic, inclined, and eccentric orbits, we have

$$\max_n |F_{2mkn}| \approx |F_{2m\tilde{n}}|. \quad (4.14)$$

An example is shown in Fig. 3. Reproducing Fig. 3 under the same conditions but with an orbital inclination of  $\theta_{\text{inc}} = 70^\circ$  shifts the peaks occur to  $n \simeq 35$ . It is somewhat remarkable that the Peters-Mathews result can be used to predict the peak locations in this way, since the generic Kerr orbits considered here do not closely resemble the analogous Keplerian orbits either in their orbital frequencies or in their shapes. We note that while the Peters-Mathews power formula (4.11) gives reasonable estimates for the location in  $n$  of the dominant modes, it does not accurately predict the actual flux associated with the dominant modes (for example, the top panel of Fig. 14 in Ref. [2] shows a very narrow peak when compared to the relatively broad peak for the  $e = 0.7$  orbit in Fig. 3 from Ref. [66]).

It is likely that the  $l > 2$  analog of the Peters-Mathews power formula (4.11) would be a useful estimator of the values of the radial harmonic index  $n$  for the dominant modes. Such an estimator would be valuable tool for designing a more accurate truncation scheme for the sums

over  $n$ . The value of  $n$  for the dominant modes  $F_{lmkn}$  increases roughly linearly with  $l$ , so it may be possible to “track” the peak location starting from the Peters-Mathews power formula (4.11) at  $l = 2$ . Future progress along these lines may reduce the limitations of our code for computing accurate fluxes for highly eccentric orbits.

#### D. Validation

We have compared the output of our code with two existing codes. The first, the “circular code” by Hughes [1], treats orbits which have a non-zero inclination and a constant radius. The second, the “equatorial code” by Glampedakis and Kennefick [2], treats orbits which are eccentric and confined to the equatorial plane. Both of these codes have already passed a variety of tests of their own (described below, but see Refs. [1, 2] for more details). Also, the circular and equatorial codes have been shown to agree with each other for orbits which are both circular and equatorial [2].

The circular code has been shown to agree with analytical post-Newtonian approximations, found in Ref. [59], in the weak field limit. It has also been shown to have the correct rotational properties in the Schwarzschild limit (see Sec. V B of Ref. [1] for details). Our code is a direct descendant of the circular code, and it has some elements in common with that code. Namely, both use the same routines for solving the homogeneous radial equation, and also for solving the angular equation. However, they differ in their methods for solving the geodesic equations, in their methods for computing the quantities  $Z_{lmkn}^*$ , and in their methods for truncating the sums representing the fluxes. When computing the individual modes  $\langle dX/dt \rangle_{lmkn}^{H,\infty}$  (for  $X = E, L_z$ ) with our code and the circular code, we find differences  $\Delta \langle dX/dt \rangle_{lmkn}^{H,\infty} \lesssim (10^{-5}) \langle dX/dt \rangle_{lmkn}^{H,\infty}$ . Here we are comparing the difference to the total flux rather than the mode itself because often there can be large fractional disagreements for insignificant modes. When computing the total fluxes  $\langle dX/dt \rangle^{H,\infty}$  with these two codes, we find differences  $\Delta \langle dX/dt \rangle^{H,\infty} \lesssim (10^{-5}) \langle dX/dt \rangle^{H,\infty}$ .

The equatorial code has been tested against its own direct ancestors [32, 68], against the circular code, and also against Shibata’s earlier equatorial code [35]. Note that in the case of the test against Shibata’s code, Glampedakis and Kennefick found agreement only at a level of about 1%. Shibata has since reported that after improving his code, he now agrees with Glampedakis and Kennefick to much greater accuracy [69]. When computing the individual modes  $\langle dX/dt \rangle_{lmkn}^{H,\infty}$  (for  $X = E, L_z$ ) our code always agrees with the equatorial code at the level of the equatorial code’s claimed fractional accuracy of  $10^{-3}$ . We have tested this for the top panels of Figs. 14-16 of Ref. [2]; by fractional accuracy, we mean the ratio of the differences in modes to the sum of all the modes shown in each of the figures. When computing the

total fluxes  $\langle dX/dt \rangle$  we find that our code always agrees with the equatorial code at the level of their claimed fractional accuracy of  $10^{-3}$ . We have tested this for the top panel, for  $a = 0.5$ , of Table VII of Ref. [2]. Note that the fractional accuracy of  $10^{-3}$  is the most conservative of the accuracy claims made in Ref. [2]. Usually we find agreement with the equatorial code well beyond this figure; for many of the total fluxes, we agree with all six of their published digits.

While we find agreement with the equatorial code when computing the *total* fluxes  $\langle dX/dt \rangle$ , the two codes show significant differences when computing the horizon fluxes  $\langle dX/dt \rangle^H$  (no such disagreement was found for the fluxes at infinity  $\langle dX/dt \rangle^\infty$ ). The disagreement is especially strong for the energy flux at the horizon, but it is also present to a lesser extent with the angular momentum flux at the horizon. For the energy fluxes at the horizon, we typically only agree with the equatorial code to about 1-10%, however in one case (the orbit with  $e = 0.4$  and  $p = 5$  in Table VII of Ref. [2], which has an exceptionally weak energy flux at the horizon) our results differ fractionally by about a factor of three, and they even have different signs. Currently the source of this disagreement is unknown. We emphasize however that the total flux of either energy or angular momentum is always dominated by the flux at infinity, and even in the most extreme case of our disagreements over the horizon fluxes, we still find acceptable agreement for the total fluxes.

Hughes has shown that, in the Schwarzschild limit, under a transformation from an equatorial to an inclined orbit, the individual modes must transform as [1]<sup>12</sup>

$$\frac{\langle dE/dt \rangle_{l(m-k)kn}^*(\theta_{\text{inc}})}{\langle dE/dt \rangle_{lm0n}^*(\theta_{\text{inc}} = 0)} = \left| \mathcal{D}_{(m-k)m}^l(\theta_{\text{inc}}) \right|^2, \quad (4.15)$$

where  $\mathcal{D}_{m'm}^l(\theta_{\text{inc}})$  is the Wigner D-function, as defined by Eq. (4.256) in Ref. [55]:

$$\begin{aligned} \mathcal{D}_{m'm}^l(\theta_{\text{inc}}) &= \sum_{q=\max(0, m'-m)}^{\min(l-m, l+m')} (-1)^q \\ &\times \left( \cos \frac{\theta_{\text{inc}}}{2} \right)^{2l+m'-m-2q} \left( -\sin \frac{\theta_{\text{inc}}}{2} \right)^{m-m'+2q} \\ &\times \frac{\sqrt{(l+m')!(l-m')!(l+m)!(l-m)!}}{q!(l-m-q)!(l+m'-q)!(m-m'+q)!}. \end{aligned} \quad (4.16)$$

For a variety of generic Schwarzschild orbits (which are both eccentric and inclined) and for a variety of modes, we have checked that our code satisfies this requirement to a fractional accuracy of  $10^{-5}$  or better. We have also confirmed that, again for a variety of generic Schwarzschild orbits, the total fluxes of energy at both the horizon and infinity, are independent of inclination

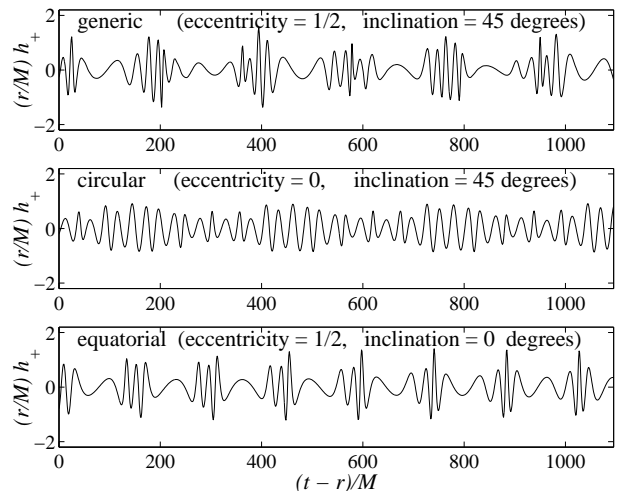


FIG. 4: A comparison of waveforms associated with a generic orbit and with the related circular and equatorial orbits. Each orbit has a semilatus rectum of  $p = 4$ . The magnitude of the massive black hole’s spin angular momentum is  $aM = 0.9M^2$ . Each waveform is plotted for  $1.5 \times M/(10^6 M_\odot)$  hours as seen from a viewing angle of  $\theta = 30^\circ$  away from the symmetry axis of the massive black hole.

(we have checked this up to a fractional accuracy of  $10^{-4}$ ).

With the help of Norichika Sago, we have also compared the output of our code with analytical post-Newtonian expressions (essentially an extension of Ref. [59]) for the fluxes of energy and angular momentum at infinity for orbits which are both slightly eccentric and slightly inclined [70]. We compared the contributions for  $l = 2, 3$ , and 4. With a requested accuracy of  $10^{-4}$  in our numerical code, the two methods of calculation always agreed to  $\sim 10^{-3}$  or better (with slightly better agreement for angular momentum fluxes than for energy fluxes). Preliminary investigations suggest that this disagreement is due to the small-eccentricity-expansion used when deriving the post-Newtonian expressions, and is therefore not unexpected.

## V. RESULTS

In this section we discuss the results found from using the code described in the previous section. After describing the general characteristics of the radiation from a typical generic orbit, we will discuss how these characteristics vary over a catalog of orbits.

### A. Radial and polar voices

Figure 4 compares a snapshot waveform produced by a generic orbit with the waveforms produced by the circular and equatorial limits of that orbit. It is clear that the generic waveform is not well approximated by either

<sup>12</sup> Here we correct two typos in Eq. (5.4) of Ref. [1].

of the limiting cases at the level of accuracy needed to produce detection waveforms (fractional phase accuracy of  $\sim 10^{-4}$ ). We can however understand the generic waveform as a composition of the effects produced by the different components of the orbital motion: the polar motion  $\theta(\lambda)$  and the radial motion  $r(\lambda)$ . To do so, we first define the general waveform quantity

$$H = h_+ - ih_\times = \sum_{kn} H_{kn} e^{-i\omega_{kn}(t-r)}, \quad (5.1)$$

where

$$H_{kn} = -\frac{2}{r} \sum_{lm} \frac{Z_{lmkn}^H}{\omega_{mkn}^2} S_{lmkn}(\theta) e^{im[\phi - \Omega_\phi(t-r)]}, \quad (5.2)$$

$$\omega_{kn} = k\Omega_\theta + n\Omega_r. \quad (5.3)$$

Each term  $H_{kn} \exp[-i\omega_{kn}(t-r)]$  in the sum (5.1) can be likened to a ‘‘voice’’ in the GW produced by the orbit. By using the general expression for the  $Z_{lmkn}^*$  coefficients (3.50) and the symmetry rules (2.24) for the geodesic expansions, we see that in the limiting circular and equatorial cases, only some voices contribute

$$H_{kn} \propto \delta_{n0}, \quad (\text{circular orbits}) \quad (5.4a)$$

$$H_{kn} \propto \delta_{k0}, \quad (\text{equatorial orbits}) \quad (5.4b)$$

$$H_{kn} \propto \delta_{n0}\delta_{k0}. \quad (\text{circular-equatorial orbits}) \quad (5.4c)$$

The term  $H_{00}$ , the sum of all the terms which oscillate at pure multiples of the azimuthal frequency, is the only nonvanishing term for orbits which are both circular and equatorial. The polar and radial voices are made of terms which oscillate at integer linear combinations of the azimuthal frequency, and either the radial or polar frequency. The polar voices, with  $n = 0$  and  $k \neq 0$ , can be thought of as being produced by the orbital inclination. Similarly, the radial voices ( $k = 0$  and  $n \neq 0$ ) are produced by the orbit’s eccentricity. This suggests the following separation of the voices:

$$H = H_{\text{azimuthal}} + H_{\text{polar}} + H_{\text{radial}} + H_{\text{mixed}}, \quad (5.5)$$

where

$$H_{\text{azimuthal}} = H_{00}, \quad (5.6a)$$

$$H_{\text{polar}} = \sum_{k \neq 0} H_{k0} e^{-i\omega_{k0}t}, \quad (5.6b)$$

$$H_{\text{radial}} = \sum_{n \neq 0} H_{0n} e^{-i\omega_{0n}t}, \quad (5.6c)$$

$$H_{\text{mixed}} = \sum_{k \neq 0} \sum_{n \neq 0} H_{kn} e^{-i\omega_{kn}t}. \quad (5.6d)$$

Figure 5 displays the waveforms for the different voices of the generic waveform from Fig. 4. Since that orbit has eccentricity  $e = 0.5$  and inclination  $\theta_{\text{inc}} = 45^\circ$ , one might expect that the radial and polar voices would be comparably loud. Instead (as one might guess by looking

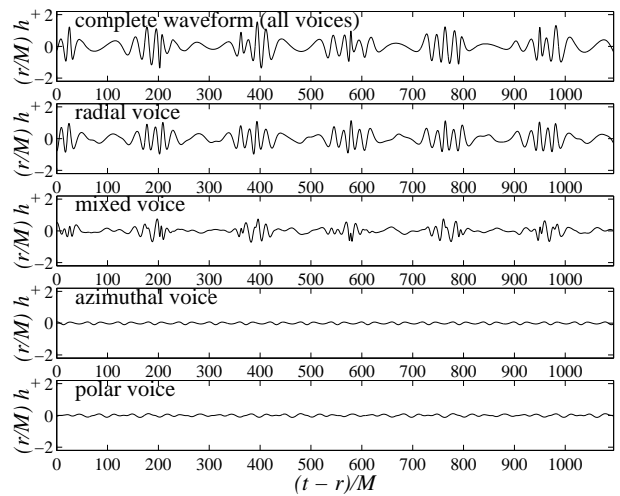


FIG. 5: The waveform from Fig. 4 and its separated pieces Eq. (5.6a). This orbit has an eccentricity  $e = 0.5$ , inclination  $\theta_{\text{inc}} = 45^\circ$ , and semilatus rectum  $p = 4$ . The spin of the black hole is  $a = 0.9M$ . We plot the waveforms as seen from a viewing angle of  $\theta = 30^\circ$ . A plot of  $h_\times$  shows similar behavior.

|                           | radial | polar | azimuthal | mixed |
|---------------------------|--------|-------|-----------|-------|
| $\langle dE/dt \rangle$   | 62%    | 1.2%  | 0.52%     | 37%   |
| $\langle dL_z/dt \rangle$ | 73%    | 0.77% | 1.0%      | 25%   |

TABLE II: The results of applying the splitting procedure described by Eq. (5.5) to the fluxes of energy  $E$  and angular momentum  $L_z$  produced by the generic orbit from Fig. 4. Each number is the ratio of the contribution from a specific voice, to the total quantity.

at the waveform from the equatorial limit of this orbit; cf. Fig. 4), the radial voice alone  $H_{\text{radial}}$  has a phase history which is similar to that of the complete waveform. The polar voice  $H_{\text{polar}}$  is comparatively unimportant.

The fluxes in energy and angular momentum can be similarly separated into radial, polar, azimuthal, and mixed pieces. Again for this case, the radial voice dominates. Table II shows how the fluxes are distributed in the case of the orbit used to produce Figs. 4 and 5. The radial voice carries away more than half of both the energy and angular momentum fluxes, while the polar voice carries only about 1%. This suggests that GWs from this orbit might, for some applications, be well approximated by its radial voice alone:  $H \approx H_{\text{radial}}$ . Such an approximation would be highly desirable since it would considerably reduce the computational cost of generating this waveform. Unfortunately  $H_{\text{radial}}$  is still quite sensitive to the orbital inclination, as can be seen by comparing to the waveforms for the circular and equatorial orbits in Fig. 4. This is because the inclination influences the values of all three orbital frequencies. So even if this approximation were valid for some range of orbits, it would not likely reduce the number of detection waveforms needed when

searching for events produced by those orbits, though it may reduce the computational cost to produce each waveform.

### B. Catalog of orbits

We now discuss the waveforms and fluxes for a catalog of generic orbits. The parameters of these orbits are shown in Table III. Tables IV and V show the relative contributions of the different voices for these waveforms.

It is clear that as inclination is increased, radiation is channeled into the polar voice, and that likewise the radial voice is amplified by an increase in eccentricity. Although both voices can be amplified by such adjustments, the radial voice seems particularly booming while the polar voice is more subtle. While the polar voice can be made dominant, it requires especially low eccentricity, below about 0.3. Also, for orbits with eccentricity as low as 0.1 and inclinations  $\theta_{\text{inc}} \lesssim 45^\circ$  or  $\theta_{\text{inc}} \gtrsim 135^\circ$ , one should expect to capture at least half of the radiative power and torque in the azimuthal voice alone. This is especially significant since the azimuthal voice is *exceedingly* inexpensive to compute in comparison to the others. It is composed only of oscillations at pure multiples of the azimuthal frequency with  $k = n = 0$ , so that computing it alone would mean replacing all of the four dimensional sums in Sec. III D with only two dimensional sums.

The asymptotic energy and angular momentum fluxes associated with the catalog (Table III) are displayed in Tables VI and VII. The energy and angular momentum fluxes were requested to have fractional accuracies of  $\varepsilon_{\text{flux}} = 10^{-4}$ . The estimates of the actual fractional accuracies, shown in square brackets in Tables VI and VII, were determined as follows: First we compute each flux with a requested fractional accuracy of  $\varepsilon_{\text{flux}} = 10^{-4}$ . The fractional accuracy claimed in Tables VI and VII is then either  $10^{-4}$ , or if larger, the fractional residual that was found when comparing with the same flux computed with a requested fractional accuracy of  $\varepsilon_{\text{flux}} = 10^{-3}$ . The summation buffer  $B$  for the polar harmonic index  $k$  is 3, while  $B = 5$  for the radial harmonic index  $n$ . The largest  $l$  value needed for the  $e = 0.1, 0.3$  orbits was  $l = 10$ , while for the  $e = 0.5, 0.7$  orbits the largest  $l$  value was  $l = 11$ . The most complex waveform,  $(e, \theta_{\text{inc}}) = (0.7, 80^\circ)$ , is made up of about 160,000 modes (about 80,000 mode calculations due to symmetry). The simplest waveform,  $(e, \theta_{\text{inc}}) = (0.1, 20^\circ)$ , is made from about 17,000 modes (about 8,500 mode calculations).

Some examples of waveforms are finally shown in the time domain in Figs. 6. There we plot  $h_+$  waveforms for  $3 \times M/(10^6 M_\odot)$  hours as seen from four different viewing angles  $\theta = 0^\circ, 30^\circ, 60^\circ, 90^\circ$ . These plots show that the radial voice has a burst-like character, while the polar voice is more of a modulated hum. These features are consistent with the characteristics found in earlier work

which focused on circular orbits [1] and on equatorial orbits [2].

## VI. SUMMARY AND FUTURE WORK

This work describes the first calculation of gravitational waves, and asymptotic radiative fluxes of energy and axial angular momentum, produced by a spinless test mass on a generic bound geodesic of a spinning black hole. It represents the natural extension of the earlier works shown in Table I. The future direction of this work is rather straightforward: fill in the last checkmark in Table I by implementing an evolution scheme for the constants of the geodesic orbits, and in particular for the Carter constant. Our anticipated path toward this goal is discussed in more detail in Ref. [6]. Once completed, we will be able to compute generic inspiral waveforms which will facilitate the initial detection of EMRIs. Completing this program will require implementing Mino's scheme for evolving the Carter constant into equations which can be entered directly into a code [5, 6, 7, 8]. It will also require a variety of more computational tasks, such as developing a dynamical scheme for artificially zeroing badly behaved modes as described in Secs. IV C and IV B. We are optimistic about completing this program since most of the remaining work is relatively straightforward in the sense that there are no known potentially overwhelming hurdles.

### Acknowledgments

We thank Marc Favata, Étienne Racine, Saul Teukolsky, and especially Éanna Flanagan for helpful discussions. We also thank Enrico Barausse for identifying several typographical errors in equations contained in the appendices of an earlier version of this manuscript. We are particularly grateful to Kostas Glampedakis and Daniel Kennefick for providing data that allowed us to compare results with their code [2], and to Norichika Sago for comparing some of our generic fluxes with analytical post-Newtonian approximations [70]. We also thank Eric Poisson, Adam Pound, and Bernhard Nickel for providing an advance draft of Ref. [43] to us, and Eric Poisson for extensive discussion regarding the importance of the conservative self force. S.D. would like to thank Takahiro Tanaka, Kyoto University, and the Yukawa Institute for Theoretical Physics, for hospitality during the final stages of editing this manuscript. This work was supported at Cornell by NSF Grants PHY-0140209 and PHY-0457200, and the NASA/New York Space Grant Consortium, and at MIT by NASA Grant NAGW-12906 and NSF Grant PHY-0244424. Part of this research was carried out at the Jet Propulsion Laboratory, California Institute of Technology, under a contract with the National Aeronautics and Space Administration and funded

| $e$ | $p$ | $\theta_{\text{inc}}$ | $E/\mu$        | $L_z/(\mu M)$   | $Q/(\mu^2 M^2)$ |
|-----|-----|-----------------------|----------------|-----------------|-----------------|
| 0.1 | 6   | 20°                   | 0.923976142907 | 2.65115182126   | 0.944969071904  |
| 0.1 | 6   | 40°                   | 0.926051429284 | 2.22165013064   | 3.52285570065   |
| 0.1 | 6   | 60°                   | 0.929863620985 | 1.52003893228   | 7.01378240707   |
| 0.1 | 6   | 80°                   | 0.935903446174 | 0.564178168635  | 10.3350037833   |
| 0.1 | 12  | 100°                  | 0.962956523141 | -0.701069332316 | 15.8653948211   |
| 0.1 | 12  | 120°                  | 0.963964137935 | -2.07109099890  | 12.9112484603   |
| 0.1 | 12  | 140°                  | 0.964900141027 | -3.24526311278  | 7.43835020273   |
| 0.1 | 12  | 160°                  | 0.965574148307 | -4.04295255570  | 2.17176613884   |
| 0.3 | 6   | 20°                   | 0.929683266598 | 2.66499623815   | 0.953716658814  |
| 0.3 | 6   | 40°                   | 0.931463021604 | 2.23504604006   | 3.56152665553   |
| 0.3 | 6   | 60°                   | 0.934742155317 | 1.53133514084   | 7.11166313087   |
| 0.3 | 6   | 80°                   | 0.939961770755 | 0.569540184106  | 10.5245453291   |
| 0.3 | 12  | 100°                  | 0.965665301518 | -0.704444574360 | 16.0138725377   |
| 0.3 | 12  | 120°                  | 0.966529280028 | -2.08286664248  | 13.0549867002   |
| 0.3 | 12  | 140°                  | 0.967333822046 | -3.26633491912  | 7.53338516325   |
| 0.3 | 12  | 160°                  | 0.967914357052 | -4.07155287011  | 2.20208170741   |
| 0.5 | 6   | 20°                   | 0.941309757948 | 2.69327096428   | 0.971725840431  |
| 0.5 | 6   | 40°                   | 0.942555891555 | 2.26253463210   | 3.64161734490   |
| 0.5 | 6   | 60°                   | 0.944866295222 | 1.55467904187   | 7.31622158779   |
| 0.5 | 6   | 80°                   | 0.948580242140 | 0.580718189662  | 10.9253034674   |
| 0.5 | 12  | 100°                  | 0.971221837220 | -0.711332909044 | 16.3190869455   |
| 0.5 | 12  | 120°                  | 0.971826517606 | -2.10697070044  | 13.3517251785   |
| 0.5 | 12  | 140°                  | 0.972392433557 | -3.30957999464  | 7.73032698828   |
| 0.5 | 12  | 160°                  | 0.972802509120 | -4.13035470435  | 2.26507351639   |
| 0.7 | 6   | 20°                   | 0.959306993445 | 2.73722358422   | 1.00010433263   |
| 0.7 | 6   | 40°                   | 0.959910828459 | 2.30561707530   | 3.76913698051   |
| 0.7 | 6   | 60°                   | 0.961041797423 | 1.59171983094   | 7.64712824881   |
| 0.7 | 6   | 80°                   | 0.962889252972 | 0.598733562204  | 11.5872341739   |
| 0.7 | 12  | 100°                  | 0.979920978103 | -0.722026359625 | 16.7987400685   |
| 0.7 | 12  | 120°                  | 0.980213741124 | -2.14458473041  | 13.8215334684   |
| 0.7 | 12  | 140°                  | 0.980489898895 | -3.37737131644  | 8.04421001469   |
| 0.7 | 12  | 160°                  | 0.980691338739 | -4.22282649751  | 2.36594094475   |

TABLE III: Each row above describes an orbit in our catalog. The numbers to the right hand side of the vertical bar were computed (to an fractional accuracy of  $10^{-12}$ ) from the numbers on the left hand of the bar (using the method described in Appendix A). Each orbit has  $a = 0.9M$ .

through the internal Research and Technology Development program.

## APPENDIX A: GEODESIC DETAILS

The functions  $V_t$ ,  $V_r$ ,  $V_\theta$ , and  $V_\phi$  appearing in the geodesic equations (2.4) are given by [3, 4]:

$$V_t(r, \theta) = E \left( \frac{\varpi^4}{\Delta} - a^2 \sin^2 \theta \right) + aL_z \left( 1 - \frac{\varpi^2}{\Delta} \right), \quad (\text{A1a})$$

$$V_r(r) = (E\varpi^2 - aL_z)^2 - \Delta [\mu^2 r^2 + (L_z - aE)^2 + Q], \quad (\text{A1b})$$

$$V_\theta(\theta) = Q - L_z^2 \cot^2 \theta - a^2(\mu^2 - E^2) \cos^2 \theta, \quad (\text{A1c})$$

$$V_\phi(r, \theta) = L_z \csc^2 \theta + aE \left( \frac{\varpi^2}{\Delta} - 1 \right) - \frac{a^2 L_z}{\Delta}, \quad (\text{A1d})$$

| $e$ | $\theta_{\text{inc}}$ | $\mathcal{P}_{\text{radial}}$ | $\mathcal{P}_{\text{polar}}$ | $\mathcal{P}_{\text{azimuthal}}$ | $\mathcal{P}_{\text{mixed}}$ | $\mathcal{T}_{z,\text{radial}}$ | $\mathcal{T}_{z,\text{polar}}$ | $\mathcal{T}_{z,\text{azimuthal}}$ | $\mathcal{T}_{z,\text{mixed}}$ |
|-----|-----------------------|-------------------------------|------------------------------|----------------------------------|------------------------------|---------------------------------|--------------------------------|------------------------------------|--------------------------------|
| 0.1 | 20°                   | 16%                           | 8.3%                         | 74%                              | 1.8%                         | 14%                             | 5%                             | 80%                                | 1%                             |
| 0.1 | 40°                   | 13%                           | 28%                          | 52%                              | 6.6%                         | 14%                             | 17%                            | 65%                                | 4%                             |
| 0.1 | 60°                   | 9.4%                          | 48%                          | 29%                              | 14%                          | 14%                             | 29%                            | 48%                                | 9.5%                           |
| 0.1 | 80°                   | 6.7%                          | 53%                          | 10%                              | 30%                          | 20%                             | 24%                            | 33%                                | 23%                            |
| 0.3 | 20°                   | 76%                           | 1.9%                         | 14%                              | 7.9%                         | 75%                             | 1.3%                           | 19%                                | 4.7%                           |
| 0.3 | 40°                   | 58%                           | 5.4%                         | 7.8%                             | 29%                          | 67%                             | 3.6%                           | 12%                                | 17%                            |
| 0.3 | 60°                   | 37%                           | 5.9%                         | 1.8%                             | 55%                          | 58%                             | 2.7%                           | 3.8%                               | 36%                            |
| 0.3 | 80°                   | 17%                           | 1.9%                         | 0.48%                            | 80%                          | 51%                             | -2.4%                          | 1.9%                               | 49%                            |
| 0.5 | 20°                   | 90%                           | 0.077%                       | 0.46%                            | 9.5%                         | 93%                             | 0.083%                         | 0.92%                              | 6%                             |
| 0.5 | 40°                   | 66%                           | 0.24%                        | 0.64%                            | 33%                          | 77%                             | 0.18%                          | 1.5%                               | 21%                            |
| 0.5 | 60°                   | 39%                           | 0.93%                        | 1.1%                             | 59%                          | 58%                             | 0.68%                          | 3.3%                               | 38%                            |
| 0.5 | 80°                   | 19%                           | 1.6%                         | 0.0055%                          | 80%                          | 53%                             | -2%                            | 0.029%                             | 49%                            |
| 0.7 | 20°                   | 90%                           | 0.057%                       | 0.62%                            | 9.3%                         | 92%                             | 0.1%                           | 2.3%                               | 6%                             |
| 0.7 | 40°                   | 67%                           | 0.22%                        | 0.36%                            | 33%                          | 77%                             | 0.35%                          | 1.5%                               | 21%                            |
| 0.7 | 60°                   | 40%                           | 0.19%                        | 0.0018%                          | 59%                          | 61%                             | -0.17%                         | 0.0094%                            | 39%                            |
| 0.7 | 80°                   | 19%                           | 0.16%                        | 0.043%                           | 81%                          | 53%                             | -0.47%                         | 0.33%                              | 47%                            |

TABLE IV: Here we show the results of applying the splitting procedure described by Eq. (5.5) to the fluxes of energy  $E$  and angular momentum  $L_z$  produced by our catalog of generic orbits (Table III). The symbol  $\mathcal{P}$  represents a ratio of the average power relative to the total average power  $\langle dE/dt \rangle$ , and the symbol  $\mathcal{T}$  represents a ratio of the average torque to the total average torque  $\langle dL_z/dt \rangle$ . Each of these orbits has  $a = 0.9M$  and  $p = 6$ .

| $e$ | $\theta_{\text{inc}}$ | $\mathcal{P}_{\text{radial}}$ | $\mathcal{P}_{\text{polar}}$ | $\mathcal{P}_{\text{azimuthal}}$ | $\mathcal{P}_{\text{mixed}}$ | $\mathcal{T}_{z,\text{radial}}$ | $\mathcal{T}_{z,\text{polar}}$ | $\mathcal{T}_{z,\text{azimuthal}}$ | $\mathcal{T}_{z,\text{mixed}}$ |
|-----|-----------------------|-------------------------------|------------------------------|----------------------------------|------------------------------|---------------------------------|--------------------------------|------------------------------------|--------------------------------|
| 0.1 | 100°                  | 1.1%                          | 76%                          | 7.7%                             | 15%                          | 7.8%                            | 23%                            | 67%                                | 1.3%                           |
| 0.1 | 120°                  | 4%                            | 60%                          | 22%                              | 14%                          | 7.4%                            | 35%                            | 51%                                | 6.5%                           |
| 0.1 | 140°                  | 10%                           | 35%                          | 45%                              | 9.6%                         | 12%                             | 20%                            | 63%                                | 4.8%                           |
| 0.1 | 160°                  | 18%                           | 11%                          | 68%                              | 3.3%                         | 17%                             | 5.7%                           | 76%                                | 1.6%                           |
| 0.3 | 100°                  | 6.1%                          | 17%                          | 2.1%                             | 75%                          | 52%                             | 13%                            | 26%                                | 9.4%                           |
| 0.3 | 120°                  | 20%                           | 10%                          | 4.8%                             | 65%                          | 43%                             | 8.4%                           | 14%                                | 34%                            |
| 0.3 | 140°                  | 47%                           | 4.3%                         | 7.1%                             | 42%                          | 62%                             | 3.2%                           | 13%                                | 22%                            |
| 0.3 | 160°                  | 78%                           | 0.94%                        | 7.7%                             | 13%                          | 81%                             | 0.65%                          | 11%                                | 6.9%                           |
| 0.5 | 100°                  | 7.5%                          | 0.26%                        | 0.042%                           | 92%                          | 80%                             | 1.2%                           | 0.88%                              | 18%                            |
| 0.5 | 120°                  | 23%                           | 0.37%                        | 0.038%                           | 76%                          | 56%                             | 0.5%                           | 0.18%                              | 43%                            |
| 0.5 | 140°                  | 52%                           | 0.51%                        | 0.34%                            | 47%                          | 72%                             | 0.59%                          | 0.97%                              | 26%                            |
| 0.5 | 160°                  | 84%                           | 0.25%                        | 1.2%                             | 15%                          | 89%                             | 0.27%                          | 2.6%                               | 7.8%                           |
| 0.7 | 100°                  | 6.8%                          | 0.36%                        | 0.038%                           | 93%                          | 84%                             | 0.66%                          | 1.8%                               | 13%                            |
| 0.7 | 120°                  | 22%                           | 0.32%                        | 0.15%                            | 78%                          | 53%                             | 1%                             | 1.5%                               | 44%                            |
| 0.7 | 140°                  | 50%                           | 0.16%                        | 0.28%                            | 49%                          | 70%                             | 0.4%                           | 1.5%                               | 28%                            |
| 0.7 | 160°                  | 84%                           | 0.019%                       | 0.22%                            | 16%                          | 91%                             | 0.043%                         | 0.92%                              | 8.5%                           |

TABLE V: Identical to Table IV, except that these orbits are retrograde and have semilatus rectum  $p = 12$ .

where we have defined

$$\varpi^2 = r^2 + a^2. \quad (\text{A2})$$

We now show some explicit relations which are used to evaluate functions of the geodesics. As indicated below, these relations were first derived either by Schmidt [45] or in Ref. [44]. We reproduce them here for the sake of completeness.

When evaluated in order, the following equations de-

termine the energy  $E = \mu\tilde{E}$ , angular momentum  $L_z = \mu M\tilde{L}_z$ , and Carter constant  $Q = (\mu M)^2\tilde{Q}$  for an orbit of a given minimum radius  $\tilde{r}_1 = r_{\text{min}}/M$ , maximum radius

| $e$ | $\theta_{\text{inc}}$ | $\langle dE/dt \rangle^{\text{H}} (M/\mu)^2$ | $\langle dE/dt \rangle^{\infty} (M/\mu)^2$ | $\langle dL_z/dt \rangle^{\text{H}} M/\mu^2$ | $\langle dL_z/dt \rangle^{\infty} M/\mu^2$ | $\langle dQ/dt \rangle / (\mu^2 M)$ |
|-----|-----------------------|--|--|--|--|-------------------------------------|
| 0.1 | 20°                   | $-4.25756 \times 10^{-6} [10^{-4}]$          | $5.87399 \times 10^{-4} [10^{-4}]$         | $-6.72410 \times 10^{-5} [10^{-4}]$          | $8.53652 \times 10^{-3} [10^{-4}]$         | $6.03753 \times 10^{-3}$            |
| 0.1 | 40°                   | $-3.96692 \times 10^{-6} [10^{-4}]$          | $6.18500 \times 10^{-4} [10^{-4}]$         | $-7.76672 \times 10^{-5} [10^{-4}]$          | $7.62823 \times 10^{-3} [10^{-4}]$         | $2.39458 \times 10^{-2}$            |
| 0.1 | 60°                   | $-3.36171 \times 10^{-6} [10^{-4}]$          | $6.83855 \times 10^{-4} [10^{-4}]$         | $-1.12143 \times 10^{-4} [10^{-4}]$          | $6.07264 \times 10^{-3} [10^{-4}]$         | $5.50060 \times 10^{-2}$            |
| 0.1 | 80°                   | $-9.78653 \times 10^{-7} [10^{-4}]$          | $8.07007 \times 10^{-4} [10^{-4}]$         | $-1.90843 \times 10^{-4} [10^{-4}]$          | $3.61820 \times 10^{-3} [10^{-4}]$         | $1.25570 \times 10^{-1}$            |
| 0.3 | 20°                   | $-5.88185 \times 10^{-6} [10^{-4}]$          | $6.80432 \times 10^{-4} [10^{-4}]$         | $-7.78419 \times 10^{-5} [10^{-4}]$          | $8.62437 \times 10^{-3} [10^{-4}]$         | $6.11706 \times 10^{-3}$            |
| 0.3 | 40°                   | $-5.88820 \times 10^{-6} [10^{-4}]$          | $7.26781 \times 10^{-4} [10^{-4}]$         | $-1.00628 \times 10^{-4} [10^{-4}]$          | $7.83499 \times 10^{-3} [10^{-4}]$         | $2.46493 \times 10^{-2}$            |
| 0.3 | 60°                   | $-5.28978 \times 10^{-6} [10^{-4}]$          | $8.31504 \times 10^{-4} [10^{-4}]$         | $-1.66905 \times 10^{-4} [10^{-4}]$          | $6.48662 \times 10^{-3} [10^{-4}]$         | $5.86987 \times 10^{-2}$            |
| 0.3 | 80°                   | $-1.52779 \times 10^{-7} [10^{-4}]$          | $1.08629 \times 10^{-3} [10^{-4}]$         | $-3.46171 \times 10^{-4} [10^{-4}]$          | $4.36910 \times 10^{-3} [10^{-4}]$         | $1.48680 \times 10^{-1}$            |
| 0.5 | 20°                   | $-8.37384 \times 10^{-6} [10^{-4}]$          | $7.98857 \times 10^{-4} [10^{-4}]$         | $-9.16902 \times 10^{-5} [10^{-4}]$          | $8.34425 \times 10^{-3} [10^{-4}]$         | $5.95501 \times 10^{-3}$            |
| 0.5 | 40°                   | $-9.06408 \times 10^{-6} [10^{-4}]$          | $8.74449 \times 10^{-4} [10^{-3}]$         | $-1.38234 \times 10^{-4} [10^{-4}]$          | $7.80844 \times 10^{-3} [10^{-3}]$         | $2.46909 \times 10^{-2}$            |
| 0.5 | 60°                   | $-8.31005 \times 10^{-6} [10^{-4}]$          | $1.05986 \times 10^{-3} [10^{-3}]$         | $-2.70993 \times 10^{-4} [10^{-4}]$          | $6.92901 \times 10^{-3} [10^{-3}]$         | $6.26645 \times 10^{-2}$            |
| 0.5 | 80°                   | $5.67035 \times 10^{-6} [10^{-4}]$           | $1.67918 \times 10^{-3} [10^{-3}]$         | $-7.40721 \times 10^{-4} [10^{-4}]$          | $5.87398 \times 10^{-3} [10^{-3}]$         | $1.93149 \times 10^{-1}$            |
| 0.7 | 20°                   | $-9.34196 \times 10^{-6} [10^{-4}]$          | $7.69363 \times 10^{-4} [10^{-2}]$         | $-8.95146 \times 10^{-5} [10^{-4}]$          | $6.66378 \times 10^{-3} [10^{-2}]$         | $4.80410 \times 10^{-3}$            |
| 0.7 | 40°                   | $-1.07089 \times 10^{-5} [10^{-3}]$          | $8.70367 \times 10^{-4} [10^{-2}]$         | $-1.57713 \times 10^{-4} [10^{-4}]$          | $6.48763 \times 10^{-3} [10^{-2}]$         | $2.06958 \times 10^{-2}$            |
| 0.7 | 60°                   | $-9.23969 \times 10^{-6} [10^{-3}]$          | $1.13494 \times 10^{-3} [10^{-2}]$         | $-3.62611 \times 10^{-4} [10^{-4}]$          | $6.29440 \times 10^{-3} [10^{-2}]$         | $5.69964 \times 10^{-2}$            |
| 0.7 | 80°                   | $2.85367 \times 10^{-5} [10^{-1}]$           | $2.69226 \times 10^{-3} [10^{-1}]$         | $-1.58165 \times 10^{-3} [10^{-2}]$          | $8.25056 \times 10^{-3} [10^{-1}]$         | $2.58125 \times 10^{-1}$            |

TABLE VI: The fluxes of energy  $E$  and axial angular momentum  $L_z$  at infinity (superscript of  $\infty$ ) and through the black hole's event horizon (superscript of H) for some generic orbits. Each of these orbits has  $a = 0.9M$  and  $p = 6$ . Each number in square brackets is an order of magnitude estimate for the fractional accuracy of the preceding number. The rates of change for the Carter constant  $\langle dQ/dt \rangle$  were computed from the formula (3.62) which follows from the assumption that radiation does not change the orbital inclination. Since this is an uncontrolled approximation, the accuracy of the  $\langle dQ/dt \rangle$  figures is unknown; we include these data for comparison purposes.

| $e$ | $\theta_{\text{inc}}$ | $\langle dE/dt \rangle^{\text{H}} (M/\mu)^2$ | $\langle dE/dt \rangle^{\infty} (M/\mu)^2$ | $\langle dL_z/dt \rangle^{\text{H}} M/\mu^2$ | $\langle dL_z/dt \rangle^{\infty} M/\mu^2$ | $\langle dQ/dt \rangle / (\mu^2 M)$ |
|-----|-----------------------|--|--|--|--|-------------------------------------|
| 0.1 | 100°                  | $1.10409 \times 10^{-8} [10^{-4}]$           | $2.50845 \times 10^{-5} [10^{-3}]$         | $-1.85760 \times 10^{-6} [10^{-4}]$          | $-1.22779 \times 10^{-4} [10^{-2}]$        | $5.64112 \times 10^{-3}$            |
| 0.1 | 120°                  | $3.80216 \times 10^{-8} [10^{-4}]$           | $2.67639 \times 10^{-5} [10^{-4}]$         | $-2.47774 \times 10^{-6} [10^{-4}]$          | $-4.91749 \times 10^{-4} [10^{-4}]$        | $6.16205 \times 10^{-3}$            |
| 0.1 | 140°                  | $7.36704 \times 10^{-8} [10^{-4}]$           | $2.83939 \times 10^{-5} [10^{-4}]$         | $-3.36034 \times 10^{-6} [10^{-4}]$          | $-8.40626 \times 10^{-4} [10^{-4}]$        | $3.86894 \times 10^{-3}$            |
| 0.1 | 160°                  | $1.06500 \times 10^{-7} [10^{-4}]$           | $2.96240 \times 10^{-5} [10^{-4}]$         | $-4.23915 \times 10^{-6} [10^{-4}]$          | $-1.09777 \times 10^{-3} [10^{-4}]$        | $1.18394 \times 10^{-3}$            |
| 0.3 | 100°                  | $2.44837 \times 10^{-8} [10^{-4}]$           | $2.92408 \times 10^{-5} [10^{-4}]$         | $-2.74782 \times 10^{-6} [10^{-4}]$          | $-1.14269 \times 10^{-4} [10^{-4}]$        | $5.32021 \times 10^{-3}$            |
| 0.3 | 120°                  | $7.99022 \times 10^{-8} [10^{-4}]$           | $3.18207 \times 10^{-5} [10^{-4}]$         | $-3.86655 \times 10^{-6} [10^{-4}]$          | $-4.92316 \times 10^{-4} [10^{-4}]$        | $6.21994 \times 10^{-3}$            |
| 0.3 | 140°                  | $1.57246 \times 10^{-7} [10^{-4}]$           | $3.45503 \times 10^{-5} [10^{-4}]$         | $-5.43045 \times 10^{-6} [10^{-4}]$          | $-8.65358 \times 10^{-4} [10^{-4}]$        | $4.01673 \times 10^{-3}$            |
| 0.3 | 160°                  | $2.32108 \times 10^{-7} [10^{-4}]$           | $3.67886 \times 10^{-5} [10^{-4}]$         | $-6.98894 \times 10^{-6} [10^{-4}]$          | $-1.15339 \times 10^{-3} [10^{-4}]$        | $1.25517 \times 10^{-3}$            |
| 0.5 | 100°                  | $6.01938 \times 10^{-8} [10^{-4}]$           | $3.44049 \times 10^{-5} [10^{-4}]$         | $-4.38711 \times 10^{-6} [10^{-4}]$          | $-9.51540 \times 10^{-5} [10^{-4}]$        | $4.56726 \times 10^{-3}$            |
| 0.5 | 120°                  | $1.87174 \times 10^{-7} [10^{-4}]$           | $3.87672 \times 10^{-5} [10^{-4}]$         | $-6.64495 \times 10^{-6} [10^{-4}]$          | $-4.68884 \times 10^{-4} [10^{-4}]$        | $6.02679 \times 10^{-3}$            |
| 0.5 | 140°                  | $3.77537 \times 10^{-7} [10^{-4}]$           | $4.37778 \times 10^{-5} [10^{-4}]$         | $-9.86398 \times 10^{-6} [10^{-4}]$          | $-8.67384 \times 10^{-4} [10^{-4}]$        | $4.09805 \times 10^{-3}$            |
| 0.5 | 160°                  | $5.75306 \times 10^{-7} [10^{-4}]$           | $4.82937 \times 10^{-5} [10^{-4}]$         | $-1.31850 \times 10^{-5} [10^{-4}]$          | $-1.20168 \times 10^{-3} [10^{-4}]$        | $1.33246 \times 10^{-3}$            |
| 0.7 | 100°                  | $1.16031 \times 10^{-7} [10^{-3}]$           | $3.29140 \times 10^{-5} [10^{-4}]$         | $-5.69490 \times 10^{-6} [10^{-4}]$          | $-6.19594 \times 10^{-5} [10^{-3}]$        | $3.14810 \times 10^{-3}$            |
| 0.7 | 120°                  | $3.48444 \times 10^{-7} [10^{-3}]$           | $3.87999 \times 10^{-5} [10^{-2}]$         | $-9.38008 \times 10^{-6} [10^{-3}]$          | $-3.67910 \times 10^{-4} [10^{-2}]$        | $4.86316 \times 10^{-3}$            |
| 0.7 | 140°                  | $7.27850 \times 10^{-7} [10^{-4}]$           | $4.62297 \times 10^{-5} [10^{-2}]$         | $-1.49671 \times 10^{-5} [10^{-4}]$          | $-7.28739 \times 10^{-4} [10^{-3}]$        | $3.54271 \times 10^{-3}$            |
| 0.7 | 160°                  | $1.16315 \times 10^{-6} [10^{-3}]$           | $5.37734 \times 10^{-5} [10^{-2}]$         | $-2.12322 \times 10^{-5} [10^{-3}]$          | $-1.06961 \times 10^{-3} [10^{-2}]$        | $1.22235 \times 10^{-3}$            |

TABLE VII: Identical to Table VI, except that these orbits are retrograde and have semilatus rectum  $p = 12$ .

$\tilde{r}_2 = r_{\text{max}}/M$ , and orbital inclination  $\theta_{\text{inc}} = \pi/2 - \theta_{\text{min}}$ :

$$\tilde{E}^2 = \frac{\kappa\rho + 2\varepsilon\sigma - 2D\sqrt{\sigma(\sigma\varepsilon^2 + \rho\varepsilon\kappa - \eta\kappa^2)}}{\rho^2 + 4\eta\sigma}, \quad (\text{A3})$$

$$\tilde{L}_z = -\frac{g_1\tilde{E}}{h_1} + D\sqrt{\frac{g_1^2\tilde{E}^2}{h_1^2} + \frac{f_1\tilde{E}^2 - d_1}{h_1}}. \quad (\text{A4})$$

$$\tilde{Q} = z_- \left( \beta + \frac{\tilde{L}_z^2}{1 - z_-} \right). \quad (\text{A5})$$

These were derived by Schmidt in Appendix B of Ref. [45]. Here the constant  $D = \text{sgn } L_z$ , so that  $D = 1$  for a prograde orbit, and  $D = -1$  for a retrograde orbit. The other constants in these equations are defined

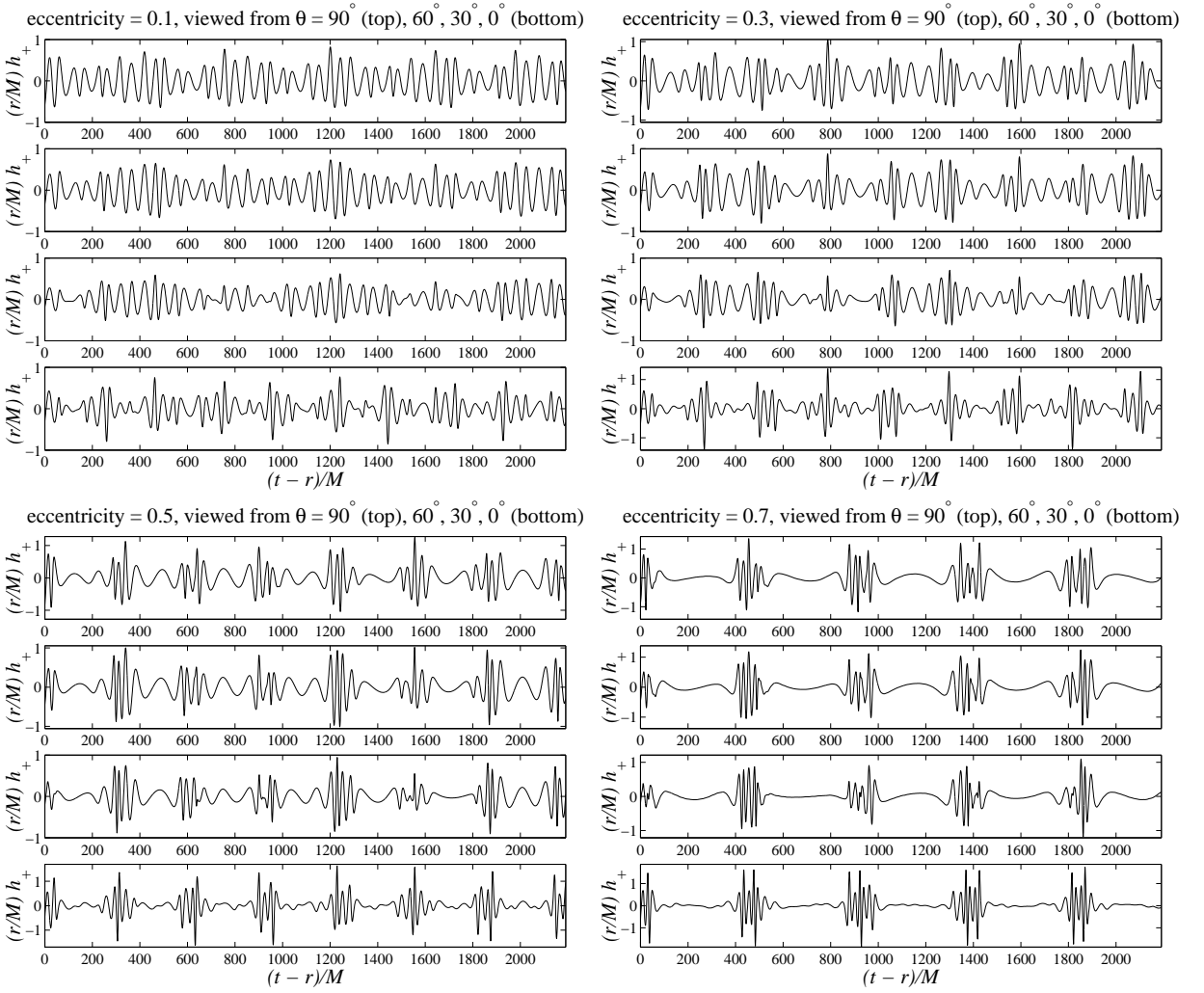


FIG. 6: Snapshot waveforms for orbits with inclination  $\theta_{\text{inc}} = 80^\circ$ , semilatus rectum  $p = 6$ , and eccentricities  $e = 0.1, 0.3, 0.5, 0.7$ . The magnitude of the black hole's spin angular momentum is  $aM = 0.9M^2$ .

in terms of the constants<sup>13</sup>

$$\tilde{a} = a/M, \quad z_- = \cos^2 \theta_{\text{min}}, \quad \beta = \tilde{a}^2(1 - \tilde{E}^2), \quad (\text{A6})$$

the functions

$$\tilde{\Delta}(\tilde{r}) = \tilde{r}^2 - 2\tilde{r} + \tilde{a}^2, \quad (\text{A7})$$

$$d(\tilde{r}) = \tilde{\Delta}(\tilde{r}^2 + z_- \tilde{a}^2), \quad (\text{A8})$$

$$f(\tilde{r}) = \tilde{r}^4 + \tilde{a}^2 [\tilde{r}(r+2) + z_- \tilde{\Delta}], \quad (\text{A9})$$

$$g(\tilde{r}) = 2\tilde{a}\tilde{r}, \quad (\text{A10})$$

$$h(\tilde{r}) = \tilde{r}(\tilde{r} - 2) + \frac{z_- \tilde{\Delta}}{1 - z_-}, \quad (\text{A11})$$

and the determinants

$$\kappa = d_1 h_2 - d_2 h_1, \quad (\text{A12})$$

$$\varepsilon = d_1 g_2 - d_2 g_1, \quad (\text{A13})$$

$$\rho = f_1 h_2 - f_2 h_1, \quad (\text{A14})$$

$$\eta = f_1 g_2 - f_2 g_1, \quad (\text{A15})$$

$$\sigma = g_1 h_2 - g_2 h_1. \quad (\text{A16})$$

A subscript 1, 2 means the function is to be evaluated at  $\tilde{r}_{1,2}$ .

<sup>13</sup> Note that Schmidt defines  $z_-$  as  $\cos \theta_{\text{min}}$  [45].

Schmidt also derives the following expressions for the

coordinate-time frequencies:

$$M\Omega_r = \frac{\pi p K(k)}{(1-e^2) \left[ (W + \tilde{a}^2 z_+ \tilde{E} X) K(k) - \tilde{a}^2 z_+ \tilde{E} X E(k) \right]}, \quad (\text{A17})$$

$$M\Omega_\theta = \frac{\pi \beta X \sqrt{z_+}}{2 \left[ (W + \tilde{a}^2 z_+ \tilde{E} X) K(k) - \tilde{a}^2 z_+ \tilde{E} X E(k) \right]}, \quad (\text{A18})$$

$$M\Omega_\phi = \frac{(Z - \tilde{L}_z X) K(k) + \tilde{L}_z X \Pi(\pi/2, z_-, k)}{(W + \tilde{a}^2 z_+ \tilde{E} X) K(k) - \tilde{a}^2 z_+ \tilde{E} X E(k)}. \quad (\text{A19})$$

Here  $k = \sqrt{z_-/z_+}$ ,

$$z_+ = \frac{\tilde{L}_z^2 + \tilde{Q} + \beta + \sqrt{(\tilde{L}_z^2 + \tilde{Q} + \beta)^2 - 4\beta Q}}{2\beta}, \quad (\text{A20})$$

$K(k)$  is the complete elliptic integral of the first kind,  $E(k)$  is the complete elliptic integral of the second kind, and  $\Pi(\phi, n, k)$  is the Legendre elliptic integral of the third kind [65]:

$$K(k) = \int_0^{\pi/2} \frac{d\theta}{\sqrt{1 - k^2 \sin^2 \theta}}, \quad (\text{A21})$$

$$E(k) = \int_0^{\pi/2} d\theta \sqrt{1 - k^2 \sin^2 \theta}, \quad (\text{A22})$$

$$\Pi(\phi, n, k) = \int_0^\phi \frac{d\theta}{(1 - n \sin^2 \theta) \sqrt{1 - k^2 \sin^2 \theta}}. \quad (\text{A23})$$

The remaining quantities in Eqs. (A17)-(A19) are defined by the following integrals:

$$W = \int_0^\pi \frac{p^2 F(\chi) d\chi}{(1 + e \cos \chi)^2 H(\chi) \sqrt{J(\chi)}} \quad (\text{A24})$$

$$X = \int_0^\pi \frac{d\chi}{\sqrt{J(\chi)}}, \quad (\text{A25})$$

$$Y = \int_0^\pi \frac{p^2 d\chi}{(1 + e \cos \chi)^2 \sqrt{J(\chi)}}, \quad (\text{A26})$$

$$Z = \int_0^\pi \frac{G(\chi) d\chi}{H(\chi) \sqrt{J(\chi)}}, \quad (\text{A27})$$

where the functions  $F, G, H, J$  are given by:

$$F(\chi) = \tilde{E} + \frac{\tilde{a}^2 \tilde{E}}{p^2} (1 + e \cos \chi)^2 - \frac{2\tilde{a}(\tilde{L}_z - \tilde{a}\tilde{E})}{p^3} (1 + e \cos \chi)^3, \quad (\text{A28})$$

$$G(\chi) = \tilde{L}_z - \frac{2}{p} (\tilde{L}_z - \tilde{a}\tilde{E}) (1 + e \cos \chi), \quad (\text{A29})$$

$$H(\chi) = 1 - \frac{2}{p} (1 + e \cos \chi) + \frac{\tilde{a}^2}{p^2} (1 + e \cos \chi)^2, \quad (\text{A30})$$

$$J(\chi) = (1 - \tilde{E}^2)(1 - e^2) + 2 \left( 1 - \tilde{E}^2 - \frac{1 - e^2}{p} \right) (1 + e \cos \chi) + \left\{ (1 - \tilde{E}^2) \frac{3 + e^2}{1 - e^2} - \frac{4}{p} + \frac{1 - e^2}{p^2} \right. \\ \left. \times \left[ \tilde{a}^2 (1 - \tilde{E}^2) + \tilde{L}_z^2 + \tilde{Q} \right] \right\} (1 + e \cos \chi)^2 \quad (\text{A31})$$

The Mino time frequencies are then found using  $\Upsilon_{\phi, \theta, r} = \Gamma \omega_{\phi, \theta, r}$ , and  $\Upsilon_\theta = \pi \sqrt{\beta z_+} / [2K(k)]$  (from Ref. [44]).

The function  $w_r(\psi)$  and its derivative were derived in the Appendix of Ref. [44]; however, there we did not write things explicitly in terms of Schmidt's  $J$ -function. The results are:

$$w_r(\psi) = \frac{1 - e^2}{p} \int_0^\psi \frac{\Upsilon_r d\psi'}{\sqrt{J(\psi')}}, \quad (\text{A32})$$

$$\frac{dw_r}{d\psi}(\psi) = \frac{1 - e^2}{p} \frac{\Upsilon_r}{\sqrt{J(\psi)}}. \quad (\text{A33})$$

The function  $w_\theta(\chi)$  and its derivative was derived in the Appendix of Ref. [44]. The results are

$$w_\theta(\chi) = \begin{cases} \Upsilon_\theta \lambda_0(\chi) & 0 \leq \chi \leq \pi/2 \\ \pi - \Upsilon_\theta \lambda_0(\pi - \chi) & \pi/2 \leq \chi \leq \pi \\ \pi + \Upsilon_\theta \lambda_0(\chi - \pi) & \pi \leq \chi \leq 3\pi/2 \\ 2\pi - \Upsilon_\theta \lambda_0(2\pi - \chi) & 3\pi/2 \leq \chi \leq 2\pi \end{cases}, \quad (\text{A34})$$

$$\frac{dw_\theta}{d\chi}(\chi) = \frac{\pi}{2K(k)} \frac{1}{1 - k^2 \cos^2 \chi}, \quad (\text{A35})$$

where

$$\lambda_0(\chi) = \frac{1}{\sqrt{\beta z_+}} [K(k) - \mathcal{F}(\pi/2 - \chi, k)], \quad (\text{A36})$$

and  $\mathcal{F}(\phi, k)$  is the incomplete elliptic integral of the first kind [65]:

$$\mathcal{F}(\phi, k) = \int_0^\phi \frac{d\theta}{\sqrt{1 - k^2 \sin^2 \theta}}. \quad (\text{A37})$$

## APPENDIX B: PERTURBATION DETAILS

The differential operators in the master equation (3.2) are given by

$$\begin{aligned} \widehat{U}_{t\phi r}(r) = & \frac{(r^2 + a^2)^2}{\Delta} \frac{\partial^2}{\partial t^2} + 4 \left[ \frac{M(r^2 - a^2)}{\Delta} - r \right] \frac{\partial}{\partial t} \\ & + \frac{a^2}{\Delta} \frac{\partial^2}{\partial \phi^2} + \frac{4a}{\Delta} (r - M) \frac{\partial}{\partial \phi} \\ & + \frac{4Mar}{\Delta} \frac{\partial^2}{\partial t \partial \phi} - \Delta^2 \frac{\partial}{\partial r} \left( \frac{1}{\Delta} \frac{\partial}{\partial r} \right), \end{aligned} \quad (\text{B1a})$$

$$\begin{aligned} \widehat{V}_{t\phi\theta}(\theta) = & -a^2 \sin^2 \theta \frac{\partial^2}{\partial t^2} - 4ia \cos \theta \frac{\partial}{\partial t} \\ & - \frac{1}{\sin^2 \theta} \frac{\partial^2}{\partial \phi^2} + 4 \frac{i \cos \theta}{\sin^2 \theta} \frac{\partial}{\partial \phi} \\ & - \frac{1}{\sin \theta} \frac{\partial}{\partial \theta} \left( \sin \theta \frac{\partial \psi}{\partial \theta} \right) + 4 \cot^2 \theta + 2. \end{aligned} \quad (\text{B1b})$$

In Boyer-Lindquist coordinates, the Kinnersly tetrad vectors are given by [1, 51]

$$\vec{l} = \frac{\varpi^2}{\Delta} \vec{\partial}_t + \vec{\partial}_r + \frac{a}{\Delta} \vec{\partial}_\phi, \quad (\text{B2a})$$

$$\vec{m} = -\frac{\rho}{\sqrt{2}} \left( ia \sin \theta \vec{\partial}_t + \vec{\partial}_\theta + \frac{i}{\sin \theta} \vec{\partial}_\phi \right), \quad (\text{B2b})$$

$$\vec{n} = \frac{\varpi^2}{2\Sigma} \vec{\partial}_t - \frac{\Delta}{2\Sigma} \vec{\partial}_r + \frac{a}{2\Sigma} \vec{\partial}_\phi, \quad (\text{B2c})$$

and the Kinnersly tetrad one-forms are

$$\tilde{l} = -\tilde{dt} + \frac{\Sigma}{\Delta} \tilde{dr} + a \sin^2 \theta \tilde{d\phi}, \quad (\text{B3a})$$

$$\tilde{m} = \frac{\rho}{\sqrt{2}} \left( ia \sin \theta \tilde{dt} - \Sigma \tilde{d\theta} - i\varpi^2 \sin \theta \tilde{d\phi} \right), \quad (\text{B3b})$$

$$\tilde{n} = -\frac{\Delta}{2\Sigma} \tilde{dt} - \frac{1}{2} \tilde{dr} + \frac{a\Delta \sin^2 \theta}{2\Sigma} \tilde{d\phi}. \quad (\text{B3c})$$

<sup>14</sup> Note that the code used in Refs. [1, 36] had the wrong prefactor for  $A_{nn0}$  (it had the factor of  $1/\bar{\rho}$  replaced with a factor of  $1/\rho$ ). Also Ref. [1] has an incorrect expression for  $A_{n\bar{m}1}$  (though this

The  $A_{abc}$  functions are given by <sup>14</sup>

$$A_{nn0} = -\frac{2\rho^{-3}\bar{\rho}^{-1}C_{nn}}{\Delta^2} \left( L_1^\dagger L_2^\dagger S + 2ia\rho L_2^\dagger S \sin \theta \right), \quad (\text{B4a})$$

$$\begin{aligned} A_{n\bar{m}0} = & -\frac{2\sqrt{2}\rho^{-3}C_{n\bar{m}}}{\Delta} \left[ \left( \frac{iK}{\Delta} - \rho - \bar{\rho} \right) L_2^\dagger S \right. \\ & \left. + \left( \frac{iK}{\Delta} + \rho + \bar{\rho} \right) ia(\rho - \bar{\rho}) S \sin \theta \right], \end{aligned} \quad (\text{B4b})$$

$$A_{\bar{m}\bar{m}0} = S\rho^{-3}\bar{\rho}C_{\bar{m}\bar{m}} \left[ \left( \frac{K}{\Delta} \right)^2 + 2i\rho \frac{K}{\Delta} + i\partial_r \left( \frac{K}{\Delta} \right) \right], \quad (\text{B4c})$$

$$A_{n\bar{m}1} = -\frac{2\sqrt{2}\rho^{-3}C_{n\bar{m}}}{\Delta} \left[ L_2^\dagger S + ia(\rho - \bar{\rho}) S \sin \theta \right], \quad (\text{B4d})$$

$$A_{\bar{m}\bar{m}1} = 2S\rho^{-3}\bar{\rho}C_{\bar{m}\bar{m}} \left( \rho - \frac{iK}{\Delta} \right), \quad (\text{B4e})$$

$$A_{\bar{m}\bar{m}2} = -S\rho^{-3}\bar{\rho}C_{\bar{m}\bar{m}}, \quad (\text{B4f})$$

where we have used the shorthand notation  $S = S_{lm}(\theta, \omega)$ . Note that the factor of  $C_{\bar{m}\bar{m}}$  in Eq. (B4c) was missing in Ref. [1] (it was not however missing from the numerical code associated with Ref. [1]).

term is correct in the code for Refs. [1, 36])

- 
- [1] S. A. Hughes, *Evolution of circular, nonequatorial orbits of Kerr black holes due to gravitational-wave emission*, Phys. Rev. D **61**, 084004 (2000); Phys. Rev. D **63**, 049902(E) (2001); Phys. Rev. D **65**, 069902(E) (2002); Phys. Rev. D **67**, 089901(E) (2003).  
[2] K. Glampedakis and D. Kennefick, *Zoom and whirl: Eccentric equatorial orbits around spinning black holes and their evolution under gravitational radiation reaction*, Phys. Rev. D **66**, 044002 (2002).  
[3] C. W. Misner, K. S. Thorne, and J. A. Wheeler, *Gravitation* (Freeman, San Francisco, 1973).  
[4] B. Carter, *Global structure of the Kerr family of gravitational fields*, Phys. Rev. **174**, 1559 (1968).

- [5] Y. Mino, *Perturbative approach to an orbital evolution around a supermassive black hole*, Phys. Rev. D **67**, 084027 (2003).  
[6] S. A. Hughes, S. Drasco, É. É. Flanagan, and J. Franklin, *Gravitational radiation reaction and inspiral waveforms in the adiabatic limit*, Phys. Rev. Lett. **94**, 221101 (2005).  
[7] S. Drasco, É. É. Flanagan, and S. A. Hughes, *Computing inspirals in Kerr in the adiabatic regime. I. The scalar case*, Class. Quantum Grav. **22**, S801 (2005).  
[8] N. Sago, T. Tanaka, W. Hikida, and H. Nakano, *Adiabatic radiation reaction to the orbits in Kerr Spacetime*, Prog. Theor. Phys., in press; gr-qc/0506092.  
[9] L. Ferrarese and D. Merritt, *A Fundamental Relation be-*

- tween Supermassive Black Holes and Their Host Galaxies, *Astrophys. J.* **539**, L9 (2000)
- [10] K. Gebhardt et al, *A Relationship between Nuclear Black Hole Mass and Galaxy Velocity Dispersion*, *Astrophys. J.* **539**, L13 (2000).
- [11] L. Spitzer, *Equipartition and the Formation of Compact Nuclei in Spherical Stellar Systems*, *Astrophys. J.* **158**, L139 (1969).
- [12] J. Miralda-Escudé and A. Gould, *A Cluster of Black Holes at the Galactic Center*, *Astrophys. J.* **545**, 847 (2000).
- [13] M. P. Muno, E. Pfahl, F. K. Baganoff, W., N. Brandt, A. Ghez, J. Lu, and M. R. Morris, *An Overabundance of Transient X-Ray Binaries within 1 Parsec of the Galactic Center*, *Astrophys. J.* **622**, L113 (2005).
- [14] M. Freitag, *Monte Carlo cluster simulations to determine the rate of compact star inspiralling to a central galactic black hole*, *Class. Quantum Grav.* **18**, 4033 (2001).
- [15] See the official NASA website <http://lisa.nasa.gov> .
- [16] See the official ESA website <http://sci.esa.int/science-e/www/area/index.cfm?fareaid=27>
- [17] J. R. Gair et al, *Event rate estimates for LISA extreme mass ratio capture sources*, *Class. Quantum Grav.* **21**, S1595 (2004).
- [18] L. Barack and C. Cutler, *LISA Capture Sources: Approximate Waveforms, Signal-to-Noise Ratios, and Parameter Estimation Accuracy*, *Phys. Rev. D* **69**, 082005 (2004).
- [19] F. D. Ryan, *Gravitational waves from the inspiral of a compact object into a massive, axisymmetric body with arbitrary multipole moments*, *Phys. Rev. D* **52**, 5707 (1995).
- [20] F. D. Ryan, *Accuracy of estimating the multipole moments of a massive body from the gravitational waves of a binary inspiral*, *Phys. Rev. D* **56**, 1845 (1997).
- [21] N. A. Collins and S. A. Hughes, *Towards a formalism for mapping the spacetimes of massive compact objects: Bumpy black holes and their orbits*, *Phys. Rev. D* **69**, 124022 (2004).
- [22] S. A. Teukolsky, *Rotating Black Holes: Separable Wave Equations for Gravitational and Electromagnetic Perturbations*, *Phys. Rev. Lett.* **29**, 1114 (1972); S. A. Teukolsky, *Perturbations of a rotating black hole. I. fundamental equations for gravitational, electromagnetic, and neutrino-field perturbations*, *Astrophys. J.* **185**, 635 (1973);
- [23] M. P. Ryan, *Teukolsky equation and Penrose wave equation*, *Phys. Rev. D* **10**, 1736 (1974).
- [24] R. Penrose, *A spinor approach to general relativity*, *Ann. Phys. (N.Y.)* **10**, 171 (1960).
- [25] S. W. Hawking and J. B. Hartle, *Energy and angular momentum flow into a black hole*, *Commun. Math. Phys.* **27**, 283 (1972).
- [26] J. B. Hartle, *Tidal Friction in Slowly Rotating Black Holes* *Phys. Rev. D* **8**, 1010 (1973); *Tidal shapes and shifts on rotating black holes* **9**, 2749 (1974).
- [27] C. Gundlach, R. H. Price, and J. Pullin, *Late-time behavior of stellar collapse and explosions. I. Linearized perturbations*, *Phys. Rev. D* **49**, 883 (1994); *Late-time behavior of stellar collapse and explosions. II. Nonlinear evolution*, **49**, 890 (1994).
- [28] C. O. Lousto and R. H. Price, *Head-on collisions of black holes: The particle limit*, *Phys. Rev. D* **55**, 2124 (1997).
- [29] K. Martel, *Gravitational waveforms from a point particle orbiting a Schwarzschild black hole*, *Phys. Rev. D* **69**, 044025 (2004).
- [30] K. Martel and E. Poisson, *One-parameter family of time-symmetric initial data for the radial infall of a particle into a Schwarzschild black hole*, *Phys. Rev. D* **66**, 084001 (2002).
- [31] C. F. Sopuerta, P. Sun, P. Laguna, and J. Xu, *A Toy Model for Testing Finite Element Methods to Simulate Extreme-Mass-Ratio-Binary Systems*, gr-qc/0507112.
- [32] C. Cutler, D. Kennefick, and E. Poisson, *Gravitational radiation reaction for bound motion around a Schwarzschild black hole*, *Phys. Rev. D* **50**, 3816 (1994).
- [33] L. S. Finn and K. S. Thorne, *Gravitational waves from a compact star in a circular, inspiral orbit, in the equatorial plane of a massive, spinning black hole, as observed by LISA*, *Phys. Rev. D* **62**, 124021 (2000).
- [34] M. Shibata, *Gravitational waves induced by a particle orbiting around a rotating black hole*, *Prog. Theor. Phys.* **90**, 595 (1993).
- [35] M. Shibata, *Gravitational waves by compact stars orbiting around rotating supermassive black holes*, *Phys. Rev. D* **50**, 6297 (1994).
- [36] S. A. Hughes, *Evolution of circular, nonequatorial orbits of Kerr black holes due to gravitational-wave emission. II. Inspiral trajectories and gravitational waveforms*, *Phys. Rev. D* **64**, 064004 (2001).
- [37] E. Poisson, *An introduction to the Lorentz-Dirac equation*, gr-qc/9912045.
- [38] P. A. M. Dirac, *Classical theory of radiating electrons*, *Proc. R. Soc. London* **A167**, 148 (1938).
- [39] Y. Mino, M. Sasaki, and T. Tanaka, *Gravitational radiation reaction to a particle motion*, *Phys. Rev. D* **55**, 3457 (1997).
- [40] T. C. Quinn and R. M. Wald, *Axiomatic approach to electromagnetic and gravitational radiation reaction of particles in curved spacetime*, *Phys. Rev. D* **56**, 3381 (1997).
- [41] E. Poisson, *The Motion of Point Particles in Curved Spacetime*, *Living Rev. Relativity* **7**, 6 (2004), <http://www.livingreviews.org/lrr-2004-6> .
- [42] A good summary of the current state and recent progress of this field can be found in a special issue of the journal *Classical and Quantum Gravity: Gravitational radiation from binary black holes: Advances in the perturbative approach*, edited by C. O. Lousto; *Class. Quantum Grav.* **22**, number 15 (2005) (Institute of Physics Publishing, Bristol, 2005).
- [43] A. Pound, E. Poisson, and B. G. Nickel, *Limitations of the adiabatic approximation to the gravitational self-force*, *Phys. Rev. D* **72**, 124001 (2005).
- [44] S. Drasco and S. A. Hughes, *Rotating black hole orbit functionals in the frequency domain*, *Phys. Rev. D* **69**, 044015 (2004).
- [45] W. Schmidt, *Celestial mechanics in Kerr spacetime*, *Class. Quant. Grav.* **19**, 2743 (2002).
- [46] M. Sasaki and T. Nakamura, *Gravitational radiation from a Kerr black hole. I*, *Prog. Theor. Phys.* **67**, 1788 (1982).
- [47] D. C. Wilkins, *Bound Geodesics in the Kerr Metric*, *Phys. Rev. D* **5**, 814 (1972).
- [48] R. H. Boyer and R. W. Lindquist, *Maximal Analytic Extension of the Kerr Metric*, *J. Math. Phys.* **8**, 265 (1967).
- [49] R. M. Wald, *On perturbations of a Kerr black hole*, *J. Math. Phys.* **14**, 1453 (1973).

- [50] E. Newman and R. Penrose, *An approach to Gravitational Radiation by a Method of Spin Coefficients*, J. Math. Phys. **3**, 566 (1962).
- [51] S. Chandrasekhar, *The Mathematical Theory of Black Holes* (Oxford University Press, New York, 1983).
- [52] E. Poisson, *Absorption of mass and angular momentum by a black hole: Time-domain formalisms for gravitational perturbations, and the small-hole/slow-motion approximation*, Phys. Rev. D **70**, 084044 (2004).
- [53] G. Khanna, *Teukolsky evolution of particle orbits around Kerr black holes in the time domain: Elliptic and inclined orbits*, Phys. Rev. D **69**, 024016 (2004).
- [54] R. Fujita and H. Tagoshi, *New Numerical Methods to Evaluate Homogeneous Solutions of the Teukolsky Equation*, Prog. Theor. Phys. **112**, 415 (2004).
- [55] G. Arfken, *Mathematical Methods for Physicists* (third edition, Academic Press, Orlando, FL, 1985).
- [56] R. A. Breuer, *Gravitational Perturbation Theory and Synchrotron Radiation*, Lecture Notes in Physics Vol. 44 (Springer-Verlag, Berlin, 1975).
- [57] M. Sasaki and H. Tagoshi, *Analytic Black Hole Perturbation Approach to Gravitational Radiation*, Living Rev. Relativity **6**, 6 (2003), <http://www.livingreviews.org/lrr-2003-6/>.
- [58] W. Kinnersly, *Type D Vacuum Metrics*, J. Math. Phys. **10**, 1195 (1969).
- [59] Y. Mino et al., *Black hole perturbation*, Prog. Theor. Phys. Suppl. **128**, 1 (1997).
- [60] R. D. Blandford and K. S. Thorne, *Applications of Classical Physics*, unpublished book, available at <http://www.pma.caltech.edu/Courses/ph136/yr2004/>, Chapt. 26.
- [61] R. A. Isaacson, *Gravitational Radiation in the Limit of High Frequency. II. Nonlinear Terms and the Effective Stress Tensor*, Phys. Rev. **166**, 1272 (1968).
- [62] S. A. Teukolsky and W. H. Press, *Perturbations of Rotating Black Hole. III. Interaction of the Hole with Gravitational and Electromagnetic Radiation*, Astrophys. J. **193**, 443 (1974).
- [63] C. Cutler, private communication.
- [64] J. Gair, private communication.
- [65] W. H. Press, S. A. Teukolsky, W. T. Vetterling, and B. P. Flannery, *Numerical Recipes in C++: The Art of Scientific Computing* (Cambridge University Press, Cambridge, 2002).
- [66] P. C. Peters and J. Mathews, *Gravitational Radiation from Point Masses in a Keplerian Orbit*, Phys. Rev. **131**, 435 (1963).
- [67] K. S. Thorne, *Multipole Expansions of Gravitational Radiation*, Rev. Mod. Phys. **52**, 299 (1980).
- [68] D. Kennefick, *Stability under radiation reaction of circular equatorial orbits around Kerr black holes*, Phys. Ref. D **58**, 064012 (1998).
- [69] M. Shibata and K. Glampedakis, private communications.
- [70] N. Sago, T. Tanaka, W. Hikida, H. Nakano, K. Ganz, *The adiabatic evolution of orbital parameters in the Kerr spacetime*, gr-qc/0511151.